Biochemical and Biophysical Research Communications 390 (2009) 1160–1166

Contents lists available at ScienceDirect

Biochemical and Biophysical Research Communications

journal homepage: www.elsevier.com/locate/ybbrc

Calyculin A-induced neurite retraction is critically dependent on actomyosin activation but not on polymerization state of microtubules

Ayumu Inutsuka, Makoto Goda, Yoshinori Fujiyoshi *

Department of Biophysics, Graduate School of Science, Kyoto University, Oiwake, Kitashirakawa, Sakyo-ku, Kyoto 606-8502, Japan

ARTICLE INFO

Article history:
Received 17 October 2009
Available online 24 October 2009

Keywords:
Actin
Myosin
Neuron
Cytoskeleton
LC-PolScope

ABSTRACT

Calyculin A (CL-A), a toxin isolated from the marine sponge *Discodermia calyx*, is a strong inhibitor of protein phosphatase 1 (PP1) and 2A (PP2A). Although CL-A is known to induce rapid neurite retraction in developing neurons, the cytoskeletal dynamics of this retraction have remained unclear. Here, we investigated the cytoskeletal dynamics during CL-A-induced neurite retraction in cultured rat hippocampal neurons, using fluorescence microscopy as well as polarized light microscopy, which can visualize the polymerization state of the cytoskeleton in living cells. We observed that MTs were bent while maintaining their polymerization state during the neurite retraction. In addition, we also found that CL-A still induced neurite retraction when MTs were depolymerized by nocodazole or stabilized by paclitaxel. These results imply a mechanism other than depolymerization of MTs for CL-A-induced neurite retraction. Our pharmacological studies showed that blebbistatin and cytochalasin D, an inhibitor of myosin II and a depolymerizer of actin, strongly inhibited CL-A-induced neurite retraction. Based on all these findings, we propose that CL-A generates strong contractile forces by actomyosin to induce rapid neurite retraction independently from MT depolymerization.

Introduction

During development of the nervous system, neurons extend and retract neurites in response to the extracellular environment to form appropriate synaptic connections. These morphological changes require the mechanical function of the cytoskeleton, particularly actin filaments and microtubules (MTs). Actin filaments are involved in force generation for neurite extension and retraction, while MTs are important for the speed of neurite outgrowth. Both of these cytoskeletal elements are dynamically rearranged in response to extracellular cues that regulate the direction and speed of neurite outgrowth [1], and are also mechanically and functionally integrated with each other [2]. However, the details of the cytoskeletal dynamics during the development of the nervous system are not well understood.

Calyculin A (CL-A) is a strong inhibitor of protein phosphatase 1 (PP1) and 2A (PP2A) [3]. It has been reported that CL-A induces actomyosin activation through myosin light chain (MLC) phosphorylation in various cells, such as smooth muscle cells [4], keratocytes [5] and sea urchin coloemocytes [6]. In rat pheochromocytoma (PC12) cells and cultured human neurons (NT 2 N cells), CL-A has also been reported to induce very rapid neurite retraction [7,8]. Merrick and coworkers attributed this retraction to MT depolymerization that was accelerated by enhanced tau phosphorylation resulting from inhibition of PP2A [8], a possibility that is in accord with the reported phosphorylation of tau by CL-A [9,10].

In this study, we directly investigated cytoskeletal dynamics during the CL-A-induced neurite retraction in young rat hippocampal neurons by employing fluorescence microscopy as well as the LC-PolScope: a special type of polarized light microscope which can depict birefringent materials such as the cytoskeleton and plasma membrane without staining or introducing fluorescent proteins. Using this system, we aimed to determine the polymerization state of the intact cytoskeleton during the retraction. We also pharmacologically examined the involvement of actin filaments and MTs in neurites during the CL-A-induced neurite retraction. Through these studies, we found that actomyosin activation is critically involved in CL-A-induced neurite retraction, and that CL-A-induced retraction is not dependent on the polymerization state of MTs.

Materials and methods

Cell cultures. Primary hippocampal neurons were prepared from embryonic day 18 rat fetuses. Hippocampi dissected from brains of the fetuses using fine forceps were treated with 0.25% trypsin for 15 min and triturated with a Pasteur pipette. The cell suspensions were plated on poly-L-lysine-coated coverslips (1×10^4 cells/cm^2)

* Corresponding author. Fax: +81 75 753 4218.
E-mail address: yoshi@em.biophys.kyoto-u.ac.jp (Y. Fujiyoshi).

0006-291X/$ - see front matter © 2009 Elsevier Inc. All rights reserved.
doi:10.1016/j.bbrc.2009.10.108

and maintained in glial-conditioned medium (Neurobasal, 2% B27 supplement, 1% L-glutamine) at 37 °C under 5% CO_2 until use. Neurobasal and B27 supplement were purchased from Invitrogen (Carlsbad, CA).

Pharmacological reagents. Blebbistatin, calyculin A and nocodazole were purchased from Sigma–Aldrich (St. Louis, MO). These reagents were dissolved in dimethylsulfoxide at 10 mM or 100 μM (calyculin A). Cytochalasin D and paclitaxel were purchased from Calbiochem (San Diego, CA), and dissolved in dimethylsulfoxide at 10 mM. These pharmacological reagents were stored at −20 °C until use.

Antibodies. Anti-acetylated tubulin antibody (Sigma–Aldrich) was diluted in blocking buffer and used in immunocytochemistry as the primary antibody. As the secondary antibody in immunocytochemistry, we used Alexa Fluor 488-conjugated anti-mouse antibody (Molecular Probes, Eugene, OR) diluted in blocking buffer.

Polarized light microscopy. The principles of the LC-PolScope were reported previously [11]. Briefly, the LC-PolScope is based on the traditional polarized light microscope, in which the crystal compensator is replaced by a universal compensator made from two liquid crystal devices (Cambridge Research Instrumentation, Cambridge, MA). The LC-PolScope enables one to obtain quantitative images of birefringent materials in living cells such as the cytoskeleton, organelles, vesicles and plasma membrane without fixation or staining. These advantages of the LC-PolScope have been exploited in live cell studies that examined the structures and functions of specific parts of cells, such as the mitotic spindle [12] and the filopodia of neural growth cones [13]. An LC-PolScope was mounted on a Nikon TE-300 inverted light microscope equipped with a PlanApo 100×/1.40 N.A. objective lens. Images were captured using a Retiga EX CCD camera (QImaging, Surrey, Canada) and analyzed using PSj software (Marine Biological Laboratory, Woods Hole, MA).

Live cell imaging. For live cell imaging, we mounted cultured neurons onto coverslips in an RC-21B closed bath chamber (Warner Instruments, Hamden, CT) and placed the chamber on the stage of a light microscope. In the chamber, neurons on the coverslip were immersed in medium heated to 37 °C by a TC-324B temperature controller (Warner Instruments). These instruments were mounted on a Nikon TE-300 inverted light microscope equipped with a PlanApo 100×/1.40 N.A. objective lens or a Leica DMR upright microscope equipped with a PlanApo 100×/1.35 N.A. objective lens. Time-lapse images of living neurons were captured using a Retiga EX CCD camera (QImaging) or iXon CCD camera (Andor Technology, Belfast, UK) and analyzed using Meta Imaging Series software (MDS Analytical Technologies, Downingtown, Pennsylvania).

Immunocytochemistry and fluorescent microscopy. Cultured neurons on coverslips were washed twice with PBS and fixed in a solution of 4% paraformaldehyde 4% sucrose/PBS for 10 min. After the fixation, the neurons were permeabilized with 0.2% Triton X-100/PBS for 10 min and blocked with 10% FBS/PBS for 1 h at room temperature. The neurons were incubated with primary antibody overnight at 4 °C and then rinsed twice with PBS, followed by secondary antibody for 1 h at room temperature. Alexa Fluor 594 phalloidin (Molecular Probes) was added to the second antibody solution to investigate the distribution of F-actin in the neurons. After the treatment with the secondary antibody, the neurons were rinsed twice with PBS, mounted on glass slides with FluorSave (Calbiochem), and observed with an Olympus BX50 fluorescence microscope equipped with 10×/0.45 N.A., 20×/0.70 N.A., 40×/0.85 N.A. or 100×/1.35 N.A UPlanApo objectives. Images of immunostained neurons on the coverslips were captured using a CoolSNAP CCD camera (Princeton Instruments, Trenton, NJ) and analyzed using Meta Imaging Series software (MDS Analytical Technologies). Primary antibodies, secondary antibodies and phalloidin were diluted in blocking buffer as follows: anti-acetylated tubulin antibody at 1:1000, Alexa Fluor 488-conjugated anti-mouse antibody at 1:500 and Alexa Fluor 594 phalloidin (Molecular Probes) at 1:50. For time-lapse imaging analyses of MTs and plasma membrane in living neurons, we employed Cellular Lights Tubulin-RFP and DiO, respectively (all the reagents were purchased from Molecular Probes). For live imaging of actin molecules in neurons, 3 μg of EGFP-actin vector, which was a kind gift from Dr. Haruhiko Bito [14], was electroporated into rat hippocampal neurons according to the manufacturer's protocol (Amaxa Inc., Gaithersburg, MD).

Neurite length analysis. For quantitative analysis of the morphological changes of cultured neurons induced by pharmacological reagents, we estimated the total neurite length of a neuron as described below. First, we labeled MTs with anti-acetylated tubulin antibody by immunocytochemistry as described above. Then, we obtained images of the neurons using an Olympus BX50 fluorescence microscope, and measured the length of each process on the fluorescence images to estimate the length of neurites in the neurons. In this analysis, the measured region on the protrusions was from the tip to the base of the process estimated from the outline of the soma (or to the branching point estimated from the outline of the process). Processes less than 10 μm long were excluded from this measurement. After the measurement, we summed up all the lengths of processes from a neuron, and defined this sum as the total neurite length of the neuron. If neurons in these fluorescence images did not have protrusions or overlapped with neighboring neurons, they were excluded from this analysis. All data are shown as mean total neurite length ± SEM ($n = 30$). Analysis of variance (ANOVA) with Scheffe's test was applied to the data to determine statistical significance by using the statistical software Excel statistics 2004 (SSRI, Tokyo, Japan).

Results

CL-A induces rapid neurite retraction in rat hippocampal neurons

We cultured rat hippocampal neurons for 2 days and then treated them with 100 nM CL-A. In line with earlier reports, this treatment induced very rapid neurite retraction within 10 min. Differential interference contrast (DIC) microscopy showed that the treatment with CL-A induced the rapid retraction of neurites to the soma (Fig. 1A). We found that this retraction had the unique characteristic that the plasma membrane kept its initial outline, in contrast to the changes that occur in the more usual neurite retraction. Lipid staining with DiO confirmed that the plasma membrane remained at the peripheral region after the retraction (Fig. 1B). If CL-A was washed out by rinsing twice with medium after the retraction, the retracted neurons formed neurites again within 1 day. The number and length of neurites increased during the subsequent days (Supplementary Material Fig. S1).

To observe the morphological features of MTs in living neurons, we employed RFP-tubulin for fluorescent microscopy. Fig. 2A shows that MTs in neurites were retracted toward the soma upon treatment with 100 nM CL-A. Note that bending of MTs occurred during the retraction (Fig. 2A). During the retraction, drastic reorganization of actin and its accumulation in the center of the soma were also observed by live imaging with EGFP-actin (Fig. 2B). EGFP-actin and RFP-tubulin visualize both free monomeric proteins and polymerized proteins, so discrimination of filamentous structures was difficult in these observations.

The LC-PolScope is a useful tool for detecting birefringence of arrayed molecules, for example, the plasma membrane and MTs in living cells, without staining or introducing fluorescent proteins

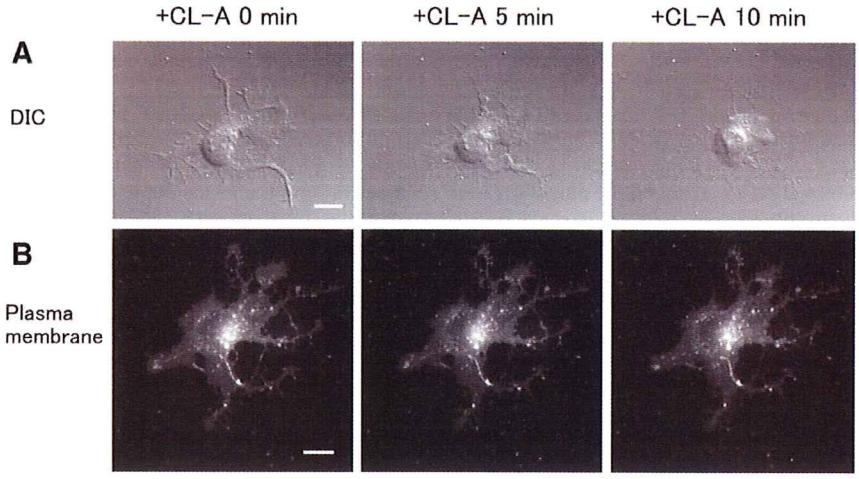

Fig. 1. Rapid neurite retraction induced by CL-A. Rat hippocampal neurons that had been cultured for 2 days were treated with 100 nM CL-A for 10 min, and sequential images of their morphological changes were observed with DIC (A) and fluorescent microscopy (B). (A) DIC images showed that cell contents in the peripheral region accumulated toward the soma, while the outline of the cell was not significantly changed. (B) Sequential fluorescence images of the plasma membrane stained with DiO revealed that the morphological features of the plasma membrane were not drastically changed. Scale bars = 10 μm.

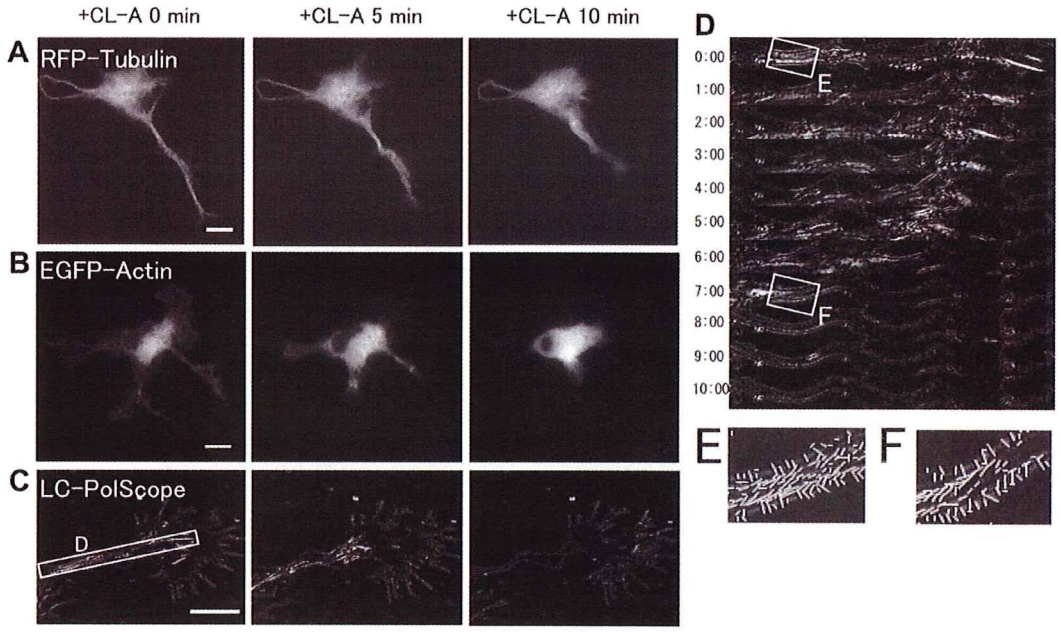

Fig. 2. Cytoskeletal reorganization during CL-A-induced neurite retraction. (A) Live-imaging of RFP-tubulin showed that MTs in neurites were bent during the retraction. (B) Fluorescence microscopy with EGFP-actin revealed that actin flowed into the soma from the peripheral region during the retraction. (C) LC-PolScope visualized birefringent materials retracting from the tip of the neurite to the soma and maintaining their birefringence during the retraction. In line with our observation in Fig. 1A, the outline of the cell was not significantly changed. (D) Montage of images (0 min–10 min) from a LC-PolScope time-lapse of the retracting MTs outlined by the white box in (C). (E,F) The magnified images in the white boxes in (D) overlaid by short lines indicating the orientations of the slow birefringence axis measured in each location. Note that the retracting MTs kept their optical property. Rat hippocampal neurons that had been cultured for 2 days were treated with 100 nM CL-A for 10 min as well as Fig. 1. Scale bars = 10 μm.

that might affect normal cell functions. The birefringence of the cytoskeleton is dependent on the polymerization state. To investigate the polymerization state of MTs in neurites during the retraction, we employed the LC-PolScope. Our observations with the LC-PolScope revealed that the signal of the birefringence of MTs was not changed remarkably during the retraction, and that the birefringent materials were retracted from the tip of the neurite to the soma without losing their birefringence (Fig. 2C and D). In addition to the magnitude of the birefringence, the LC-PolScope software can also compute the orientations of the slow birefringence axes for each image point. It was reported that the birefringence of MTs has slow axis orientations that are parallel to the fiber axis [15], while the slow axis of the cell membrane is perpendicular to the membrane axis [16]. We found that retracting MTs in the growth cone kept their slow axis orientation of their birefringence (Fig. 2E and F). These results revealed that the polymerization state of MTs was maintained during CL-A-induced neurite retraction.

Neurite retraction induced by CL-A is not dependent on MT polymerization state

The polarized light microscopic images in Fig. 2C show that marked depolymerization of MTs was not observed during the neurite retraction induced by CL-A. To further examine this, we investigated the involvement of the polymerization state of MTs in CL-A-induced neurite retraction by changing the polymerization state of MTs pharmacologically.

The LC-PolScope can clearly visualize fine structures such as veil-like lamellipodia, rod-like filopodia and the highly birefringent central domain of the growth cone which contains MTs and vesicles. Pretreatment with nocodazole (10 μM for 30 min), a depolymerizer of MTs, decreased the birefringent signal in the neurite shaft and the central domain of the growth cone (Fig. 3A). The rod-shaped birefringent materials remaining in the shaft after the nocodazole pretreatment seemed to be organelles, most likely mitochondria. This observation revealed that the pretreatment with nocodazole disrupted MT structures in neurites but did not induce retraction like that caused by treatment with CL-A. In spite of the pretreatment with nocodazole, we observed CL-A-induced neurite retraction, namely accumulation of cell contents toward the soma.

We also immunostained neurons with anti-acetylated tubulin antibody to visualize the localization of MTs and investigated the effects of a depolymerizer and a stabilizer of MTs on CL-A-induced neurite retraction. Our fluorescent microscopy and neurite length analysis revealed that pretreatment with nocodazole (10 μM, 30 min) and a stabilizer of MTs, paclitaxel (10 μM, 30 min) did not significantly affect the rearrangement of MTs induced by treatment with CL-A (Fig. 3B and C). These results revealed that CL-A-induced neurite retraction was not dependent on the polymerization state of MTs.

Actomyosin activation is critically involved in CL-A retraction

CL-A has been reported to induce actomyosin activation in various kinds of cells, and actomyosin activation is known to be

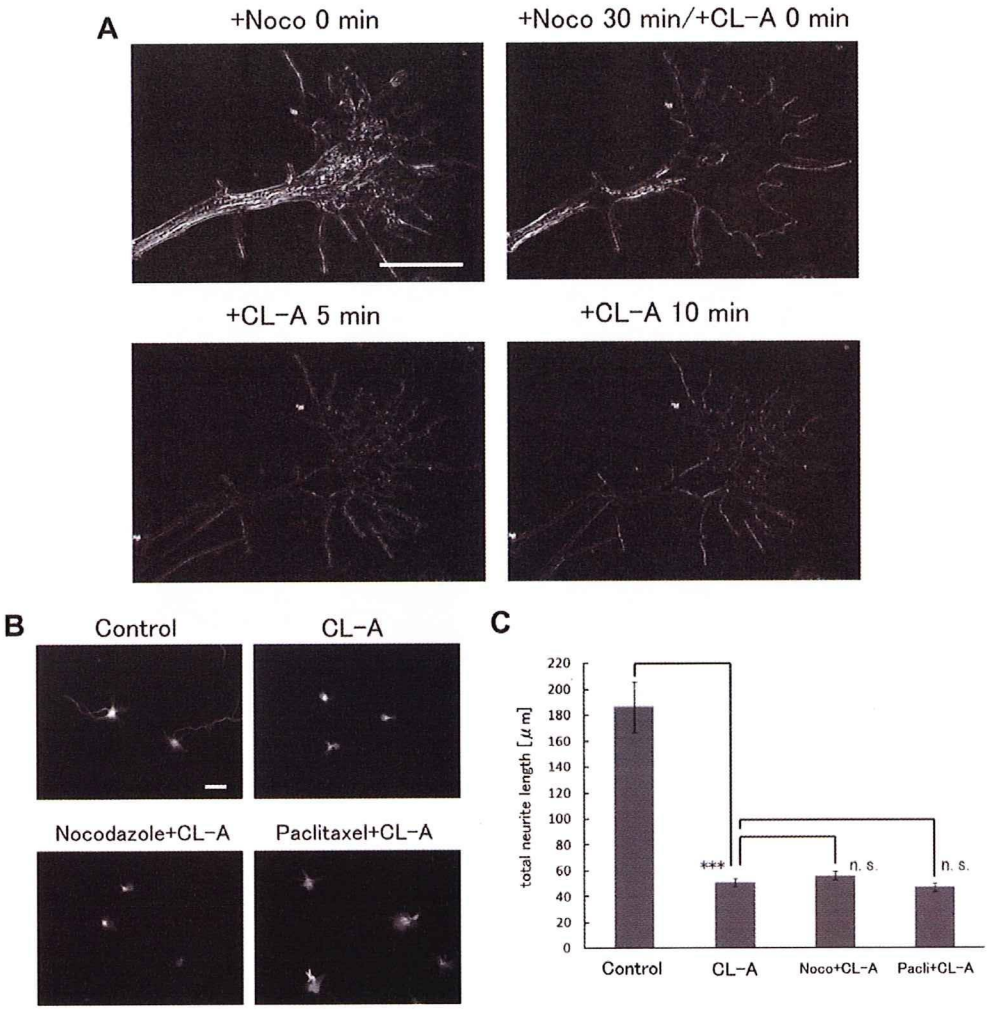

Fig. 3. Independence of CL-A-induced neurite retraction from polymerization state of MTs. (A) Neurons were pretreated with 10 μM nocodazole, a MT depolymerizer, for 30 min before treatment with 100 nM CL-A for 10 min. Sequential LC-PolScope images revealed that signals of birefringence in the growth cone and the neurite shaft were markedly weakened after the nocodazole treatment. However, CL-A induced neurite retraction despite the absence of polymerized MTs. Scale bar = 10 μm. (B) Fluorescence micrographs of neurons that had been pretreated with a MT depolymerizer, nocodazole (10 μM, 30 min), or a MT stabilizer, paclitaxel (10 μM, 30 min), and subsequently treated with CL-A (100 nM, 10 min). MTs in the neurons were labeled with anti-acetylated tubulin antibody. Scale bar = 50 μm. (C) Neurite length analyses to investigate the effects of nocodazole and paclitaxel on CL-A-induced neurite retraction. Pretreatment with nocodazole (10 μM, 10 min) or paclitaxel (10 μM, 30 min) did not significantly affect CL-A-induced neurite retraction (100 nM, 10 min). Data represent means ± SEM ($n = 30$). n.s. $P > 0.05$; $^{***}P < 0.001$, compared to CL-A.

involved in neurite retraction. In addition, our observation of bending MTs (Fig. 2A) implied that mechanical forces were induced during the CL-A-induced neurite retraction. To confirm this possibility, we investigated the involvement of actomyosin activation in the CL-A-induced neurite retraction by using a specific inhibitor of myosin II, blebbistatin, and an actin depolymerizer, cytochalasin D (CD).

Live-imaging with the LC-PolScope clearly showed that pretreatment with cytochalasin D (CD) (10 μM for 30 min) greatly decreased the birefringent signal of actin filaments in the peripheral domain of the growth cone, and shortened several filopodia, indicating that actin filaments were selectively disrupted (Fig. 3A). After this pretreatment, CL-A-induced neurite retraction was not observed within 10 min. Most of the birefringent signal in the central domain of the growth cone remained at the initial location without moving toward the soma. These results revealed that CL-A-induced neurite retraction was dependent on the polymerization state of actin filaments.

Furthermore, we stained neurons with anti-acetylated tubulin antibody and Alexa fluor 594-conjugated phalloidin to visualize the localization of actin filaments and MTs. Since phalloidin binds selectively to F-actin, the structure of actin filaments is more clearly indicated by phalloidin than EGFP-actin in Fig. 2B, which visualizes both F- and G-actin molecules. Our fluorescent microscopy and neurite length analysis revealed that pretreatment with blebbistatin (10 μM, 30 min) and CD (10 μM, 30 min) strongly inhibited the rearrangement of both actin filaments and MTs induced by treatment with CL-A (Fig. 4B and C). We confirmed that there was no significant difference in the length of neurites between untreated and blebbistatin- or CD-treated neurons. In line with our earlier observation shown in Fig. 2, CL-A treatment resulted in the radical rearrangement of both actin filaments and MTs. Note that stronger accumulation of F-actin (red) than MTs (green) was induced by the CL-A treatment, as shown in Fig. 4B (compare with those in Fig. 2B). Additionally, we confirmed that latrunculin A, another depolymerizer of actin, also inhibited CL-A-induced neurite retraction (data not shown). In summary, these results revealed that actin filaments and the motor activity of myosin II were essential for the CL-A-induced neurite retraction, and for the radical reorganization of MTs.

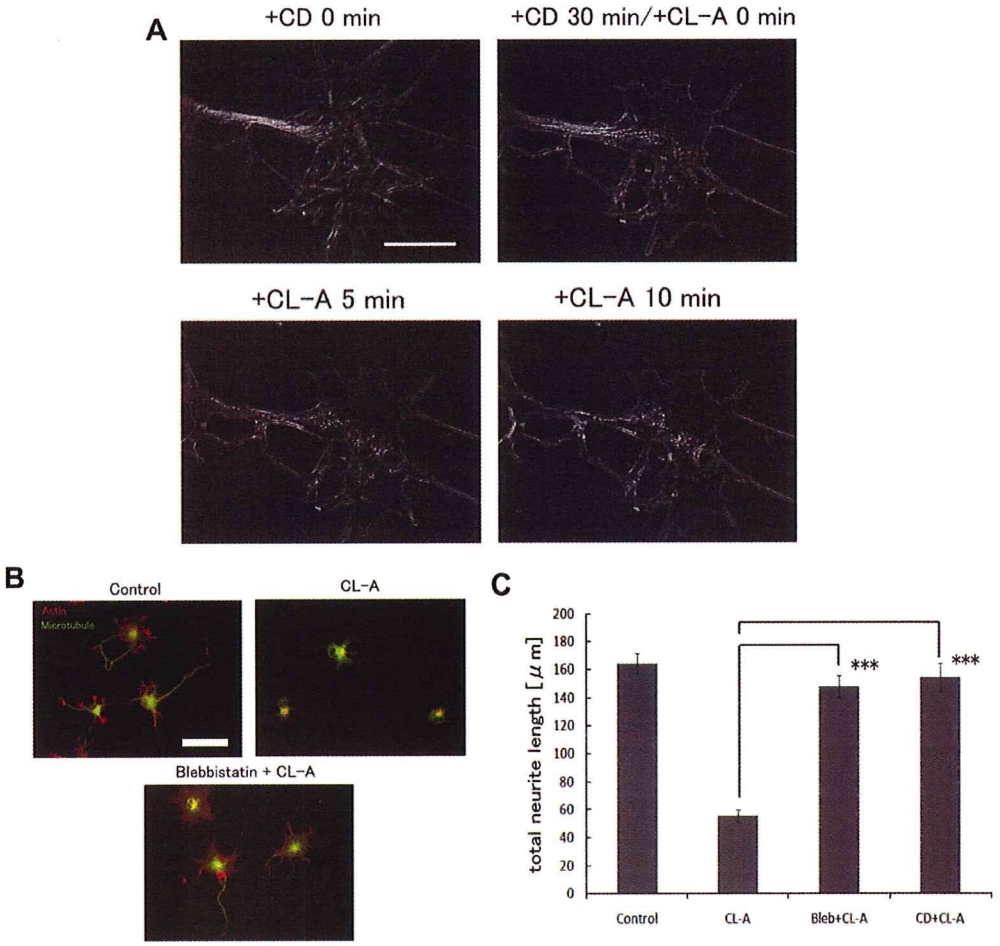

Fig. 4. Critical involvement of actomyosin activation in CL-A-induced neurite retraction. (A) Neurons were pretreated with 10 μM cytochalasin D (CD), an actin filament depolymerizer, for 30 min before treatment with 100 nM CL-A for 10 min. Sequential LC-PolScope images showed that CD weakened the birefringence of radial fibers in the growth cone, indicating that actin filaments were indeed disrupted. In the absence of actin filaments in neurons, CL-A failed to induce neurite retraction. Scale bar = 10 μm. (B) Fluorescence micrographs of neurons that had been pretreated with a myosin II inhibitor, blebbistatin (10 μM, 30 min), and were then treated with CL-A (100 nM, 10 min). Blebbistatin inhibited the rearrangement of F-actin and MTs induced by treatment with CL-A. F-actin and MTs in the neurons were labeled with Alexa Fluor 594-conjugated phalloidin and anti-acetylated tubulin antibody, respectively. Scale bar = 50 μm. (C) Neurite length analyses to investigate the effects of an inhibitor of myosin II and a depolymerizer of actin filaments on CL-A-induced neurite retraction. Pretreatment with blebbistatin (10 μM, 10 min) or cytochalasin D (10 μM, 30 min) strongly inhibited CL-A-induced neurite retraction (100 nM, 10 min). Data represent means ± SEM ($n = 30$). $^{***}P < 0.001$, compared to CL-A.

Discussion

What kind of molecular mechanism mediates the rapid neurite retraction observed in CL-A-treated neurons? A previous study reported that CL-A-induced neurite retraction resulted from MT depolymerization in cultured human neurons [8]. However, it has been reported that CL-A induces actomyosin activation in various kinds of cells [4,6], and that myosin II is involved in axon retraction of neurons induced by repulsive guidance cues such as Sema3A or lysophosphatidic acid [17,18]. In this study, the birefringence of cytoskeletal structures including MTs in neurites was shown to be maintained during CL-A-induced neurite retraction (Fig. 2C). Importantly, CL-A-induced neurite retraction was found to be independent of the MT polymerization state (Fig. 3). In contrast, CL-A-induced neurite retraction was clearly shown to be dependent on actomyosin activation. We observed that the localization of actin was altered during the retraction (Fig. 2B), and that CL-A-induced neurite retraction was dependent on the polymerization state of actin filaments or myosin II motor activity (Fig. 4). Taken together, our results strongly suggest that actomyosin activation is the main molecular mechanism of the CL-A-induced neurite retraction.

Cytoskeletal components are mechanically and functionally integrated with each other. It was reported that myosin-mediated forces are counterbalanced by dynein-mediated forces between the actin filaments and microtubule arrays in neurons [19]. Thus, it is difficult to clarify the cause-and-effect relationship between actomyosin contraction and depolymerization of MTs. We observed that CL-A treatment weakened the birefringent signal in the neurite shaft and decreased the width of the shaft after 10 min (Fig. 4A). Thus, we do not exclude the possibility that CL-A induces MT depolymerization after the retraction. Indeed, in some experiments that indicated depolymerization of MTs, samples were examined after treatment with CL-A for hours [8]. These detailed observations of the intact dynamic cytoskeletal polymerization state were unique achievements enabled by the usage of the LC-PolScope. Direct analysis of the polymerization state of the cytoskeleton using the LC-PolScope might also be utilized for the analyses of growth cone guidance by physiological guidance cues or neurite branching.

The activation of actomyosin in non-muscle cells is regulated mainly by phosphorylation of myosin light chain (MLC). Phosphorylation of MLC has been reported to be involved in neurite retraction caused by extracellular guidance cues [17,20]. We found that an inhibitor of PP1 and PP2A, okadaic acid (10 μM, 10 min), induced neurite retraction like CL-A, whereas a PP2A inhibitor, fostriecin (10 μM, 30 min) failed to induce neurite retraction (Supplementary Material Fig. S2). This might imply that CL-A inhibits myosin phosphatase, which is a PP1 and induces MLC phosphorylation. We also detected a robust increase of the di-phosphorylation of MLC at Ser19 and Thr18 by immunoblotting (Supplementary Material Fig. S3). This di-phosphorylation of MLC was not detected in neurons pretreated with a broad spectrum kinase inhibitor, staurosporine, which attenuated CL-A-induced neurite retraction (Supplementary Material Fig. S3). In smooth muscle cells and epithelial cells, it has been reported that mono-phosphorylation of MLC at Ser19 activates myosin motor activity, and that di-phosphorylation of MLC at Ser19 and Thr18 further activates myosin motor activity and induces myosin bipolar filament formation [21,22]. The strong actomyosin contraction in CL-A-induced neurite retraction might result from di-phosphorylation of MLC.

Conclusion

Our studies showed that CL-A-induced neurite retraction is critically dependent on actomyosin activation but not on the polymerization state of MTs. Polarized light microscopy revealed that MTs kept their polymerization state during the retraction. We propose that the radical reorganization of MTs in CL-A-treated neurons results from strong contractile force exerted by actomyosin.

Acknowledgments

We thank Dr. Haruhiko Bito (University of Tokyo) for EGFP-actin plasmid, Dr. Issei Mabuchi (Gakushuin University), Dr. Mio Nonaka (University of Tokyo) for helpful discussions and Dr. Elizabeth Nakajima (Kyoto University) for correcting the English of the manuscript. This work was supported by a JSPS research fellowship for young scientists; Global Center of Excellence program A06 "Formation of a Strategic Base for Biodiversity and Evolutionary Research: from Genome to Ecosystem"; Grants-in-Aid for Specially Promoted Research; and the New Energy and Industrial Technology Development Organization (NEDO).

Appendix A. Supplementary data

Supplementary data associated with this article can be found, in the online version, at doi:10.1016/j.bbrc.2009.10.108.

References

[1] B.J. Dickson, Molecular mechanisms of axon guidance, Science 298 (2002) 1959–1964.
[2] E.W. Dent, F.B. Gertler, Cytoskeletal dynamics and transport in growth cone motility and axon guidance, Neuron 40 (2003) 209–227.
[3] H. Ishihara, B.L. Martin, D.L. Brautigan, H. Karaki, H. Ozaki, Y. Kato, N. Fusetani, S. Watabe, K. Hashimoto, D. Uemura, et al., Calyculin A and okadaic acid: inhibitors of protein phosphatase activity, Biochem. Biophys. Res. Commun. 159 (1989) 871–877.
[4] H. Ishihara, H. Ozaki, K. Sato, M. Hori, H. Karaki, S. Watabe, Y. Kato, N. Fusetani, K. Hashimoto, D. Uemura, et al., Calcium-independent activation of contractile apparatus in smooth muscle by calyculin-A, J. Pharmacol. Exp. Ther. 250 (1989) 388–396.
[5] P.T. Yam, C.A. Wilson, L. Ji, B. Hebert, E.L. Barnhart, N.A. Dye, P.W. Wiseman, G. Danuser, J.A. Theriot, Actin–myosin network reorganization breaks symmetry at the cell rear to spontaneously initiate polarized cell motility, J. Cell. Biol. 178 (2007) 1207–1221.
[6] J.H. Henson, S.E. Kolnik, C.A. Fried, R. Nazarian, J. McGreevy, K.L. Schulberg, M. Detweiler, V.A. Trabosh, Actin-based centripetal flow: phosphatase inhibition by calyculin-A alters flow pattern, actin organization, and actomyosin distribution, Cell. Motil. Cytoskeleton. 56 (2003) 252–266.
[7] B.F. Reber, A. Bouron, Calyculin-A-induced fast neurite retraction in nerve growth factor-differentiated rat pheochromocytoma (PC12) cells, Neurosci. Lett. 183 (1995) 198–201.
[8] S.E. Merrick, J.Q. Trojanowski, V.M. Lee, Selective destruction of stable microtubules and axons by inhibitors of protein serine/threonine phosphatases in cultured human neurons, J. Neurosci. 17 (1997) 5726–5737.
[9] M. Bennecib, C.X. Gong, I. Grundke-Iqbal, K. Iqbal, Inhibition of PP-2A upregulates CaMKII in rat forebrain and induces hyperphosphorylation of tau at Ser 262/356, FEBS Lett. 490 (2001) 15–22.
[10] X.C. Li, Z.F. Wang, J.X. Zhang, Q. Wang, J.Z. Wang, Effect of melatonin on calyculin A-induced tau hyperphosphorylation, Eur. J. Pharmacol. 510 (2005) 25–30.
[11] R. Oldenbourg, A new view on polarization microscopy, Nature 381 (1996) 811–812.
[12] L. Liu, R. Oldenbourg, J.R. Trimarchi, D.L. Keefe, A reliable, noninvasive technique for spindle imaging and enucleation of mammalian oocytes, Nat. Biotechnol. 18 (2000) 223–225.
[13] K. Katoh, K. Hammar, P.J. Smith, R. Oldenbourg, Birefringence imaging directly reveals architectural dynamics of filamentous actin in living growth cones, Mol. Biol. Cell. 10 (1999) 197–210.
[14] T. Furuyashiki, Y. Arakawa, S. Takemoto-Kimura, H. Bito, S. Narumiya, Multiple spatiotemporal modes of actin reorganization by NMDA receptors and voltage-gated Ca^{2+} channels, Proc. Natl. Acad. Sci. USA 99 (2002) 14458–14463.
[15] R. Oldenbourg, E.D. Salmon, P.T. Tran, Birefringence of single and bundled microtubules, Biophys. J. 74 (1998) 645–654.
[16] Y. Kato, N. Fusetani, S. Matsunaga, K. Hashimoto, Calyculins, potent antitumour metabolites from the marine sponge *Discodermia calyx*: biological activities, Drugs Exp. Clin. Res. 14 (1988) 723–728.
[17] G. Gallo, RhoA-kinase coordinates F-actin organization and myosin II activity during semaphorin-3A-induced axon retraction, J. Cell. Sci. 119 (2006) 3413–3423.

[18] N. Fukushima, Y. Morita, Actomyosin-dependent microtubule rearrangement in lysophosphatidic acid-induced neurite remodeling of young cortical neurons, Brain Res. 1094 (2006) 65–75.
[19] F.J. Ahmad, J. Hughey, T. Wittmann, A. Hyman, M. Greaser, P.W. Baas, Motor proteins regulate force interactions between microtubules and microfilaments in the axon, Nat. Cell. Biol. 2 (2000) 276–280.
[20] T. Kubo, M. Endo, K. Hata, J. Taniguchi, K. Kitajo, S. Tomura, A. Yamaguchi, B.K. Mueller, T. Yamashita, Myosin IIA is required for neurite outgrowth inhibition produced by repulsive guidance molecule, J. Neurochem. 105 (2008) 113–126.
[21] M. Ikebe, J. Koretz, D.J. Hartshorne, Effects of phosphorylation of light chain residues threonine 18 and serine 19 on the properties and conformation of smooth muscle myosin, J. Biol. Chem. 263 (1988) 6432–6437.
[22] T. Watanabe, H. Hosoya, S. Yonemura, Regulation of myosin II dynamics by phosphorylation and dephosphorylation of its light chain in epithelial cells, Mol. Biol. Cell. 18 (2007) 605–616.

Journal of Structural Biology 170 (2010) 60–68

Contents lists available at ScienceDirect

Journal of Structural Biology

journal homepage: www.elsevier.com/locate/yjsbi

Structural and functional characterization of H^+,K^+-ATPase with bound fluorinated phosphate analogs

Kazuhiro Abe, Kazutoshi Tani, Yoshinori Fujiyoshi *

Department of Biophysics, Faculty of Science, Kyoto University, Oiwake, Kitashirakawa, Sakyo-ku, Kyoto 606-0852, Japan

ARTICLE INFO

Article history:
Received 22 September 2009
Received in revised form 2 December 2009
Accepted 8 December 2009
Available online 21 December 2009

Keywords:
P-type ATPase
H^+,K^+-ATPase
Two-dimensional crystal
Cryo-electron microscopy
Membrane protein structure

ABSTRACT

Gastric H^+,K^+-ATPase is responsible for gastric acid secretion. In order to characterize the phosphorylation events on H^+,K^+-ATPase, the properties of fluorinated phosphate analogs [XFs, *e.g.* aluminum fluoride (AlF), beryllium fluoride (BeF) and magnesium fluoride (MgF)], and the structural differences induced by XFs were investigated. The addition of divalent cations to the XF-inhibited H^+,K^+-ATPase restores the activity of the AlF- or MgF-inhibited, but not of the BeF-inhibited enzyme, although limited trypsin digestion reveals that they assume the same E_2P-like state. To clarify the conformational differences induced by XFs, the structure of BeF-bound H^+,K^+-ATPase was analyzed at 8 Å resolution. The structure is almost identical to the previously reported AlF-bound E_2P structure, unlike the distinctive X-ray structure of BeF-bound SERCA, in which the luminal gate was observed to be widely opened. Since the analyzed structure of the H^+,K^+-ATPase revealed that both AlF and BeF-bound to the P domain were not exposed to the solvent, the dissociation of XFs induced by divalent cations could be interpreted in terms of stability against thermal fluctuations. Furthermore, the conformational differences found between the cytoplasmic domains of H^+,K^+-ATPase and SERCA provide a framework to understand the characteristic mechanism, by which divalent cations reactivate the XF-inhibited H^+,K^+-ATPase.

1. Introduction

The highly acidic environment (pH ~1) of the animal stomach is essential for digestion and also acts as a first barrier against bacterial and viral infection. Conversely, too much acid secretion induces gastric ulcer (Wolosin, 1985; Sachs et al., 2007). The gastric proton pump, H^+,K^+-ATPase is the major membrane protein responsible for the gastric acid (H^+) secretion (Ganser and Forte, 1973). The electroneutral exchange of two cytoplasmic protons for two luminal potassium ions is achieved by the hydrolysis of one ATP molecule (Rabon and Reuben, 1990). Like other members of the cation-transporting P-type ATPase family, such as the Na^+,K^+-ATPase and the sarco(endo)plasmic reticulum Ca^{2+}-ATPase (SERCA), the enzyme undergoes cyclical conformational changes between its main reaction states, E_1 and E_2, and their phosphorylated forms, E_1P and E_2P (Post and Kume, 1973, see Fig. 1). Conformations of the enzyme that bind cations for outward transport (H^+) are defined as E_1, whereas those that bind luminal cations (K^+) are termed E_2. Proton binding to E_1 activates autophosphorylation from Mg^{2+}-ATP to form E_1P, which is soon converted to E_2P in the H^+-transporting step. Binding of K^+ to the E_2P form stimulates dephosphorylation and the transition to the occluded form $(K^+)E_2$. Subsequently, a conformational change to E_1 conformation occurs and K^+ ions are released to the cytoplasm.

The H^+,K^+-ATPase consists of two subunits. Like other highly homologous P2-type ATPases (Palmgren and Axelsen, 1998), the catalytic α-subunit contains 10 transmembrane (TM) helices (M1–M10) in which cation binding sites are located, and three cytoplasmic domains, namely, a nucleotide-binding (N), a phosphorylation (P), and an actuator (A) domains. In addition to the α-subunit, H^+,K^+- and Na^+,K^+-ATPases require an accessory β-subunit, which is indispensable for the functional expression and the trafficking of the αβ-complex to the cell surface (Chow and Forte, 1995). Furthermore, recent structural and functional analyses of the H^+,K^+-ATPase revealed important contributions of the β-subunit to the E_1P/E_2P equilibrium, which might be indispensable for enzyme activity and the large H^+ gradient generated by this pump (Dürr et al., 2008; Abe et al., 2009).

Abbreviations: H^+,K^+-ATPase, potassium-activated adenosine triphosphatase; SERCA, sarco-endoplasmic reticulum Ca^{2+} adenosine triphosphatase; Na^+,K^+-ATPase, sodium and potassium-activated adenosine triphosphatase; EP, phosphoenzyme; cryo-EM, cryo-electron microscopy; XF, fluorinated complex; AlF, aluminum fluoride; BeF, beryllium fluoride; MgF, magnesium fluoride; HEPES, *N*-2-hydroxyethylpiperazine-*N*'-2-ethanesulfonic acid; TM, transmembrane; Tris, 2-amino-2-hydroxymethyl-1,3-propanediol; MES, 4-morpholineethanesulfonic acid; SDS–PAGE, SDS–polyaclylamide gel electrophoresis.

* Corresponding author. Fax: +81 75 753 4218.
E-mail addresses: ikkei@em.biophys.kyoto-u.ac.jp (K. Abe), tani@em.biophys.kyoto-u.ac.jp (K. Tani), yoshi@em.biophys.kyoto-u.ac.jp (Y. Fujiyoshi).

1047-8477/$ - see front matter © 2009 Elsevier Inc. All rights reserved.
doi:10.1016/j.jsb.2009.12.008

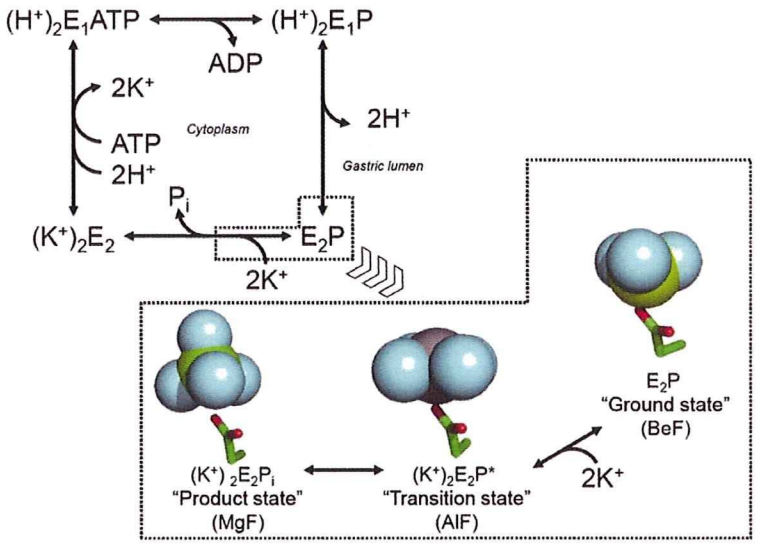

Fig. 1. Reaction scheme of H^+,K^+-ATPase and XF-induced reaction states proposed by SERCA crystal structure. Ion transport and ATP hydrolysis are coupled to the cyclic conformational conversion of the enzyme (abbreviated as "E") between its main states, E_1 and E_2, and their phosphorylation form, E_1P, E_2P. The hydrolysis of ATP generates the phosphoenzyme intermediate (E_1P, E_2P) by transfer of the γ-phosphate to the Asp386 residue of the invariant ^{386}DKTG motif in the presence of Mg^{2+} (omitted in the figure for simplicity). See Section 1 for more details. Extensive studies of SERCA with stable phosphate analogs (AlF, BeF and MgF) characterized their structural and functional properties. Namely, tetrahedral BeF shows the closest coordination of aspartylphosphate (ground state), trigonal bipyramidal AlF is assigned as a transition analog from aspartylphosphate to its hydrolysate, and tetrahedral MgF mimics inorganic phosphate produced by E_2P hydrolysis. Such subtle differences in their coordination environments generate a different type of cytoplasmic domain arrangement, thus causing distinct conformational changes of the enzyme.

Fluorinated complexes (XFs) such as aluminum fluoride (AlF), beryllium fluoride (BeF), and magnesium fluoride (MgF) are widely used to interfere with the activity of many types of enzymes. These small inorganic molecules mimic the chemical structure of phosphate (Bigay et al., 1987) and can therefore be employed for structural analysis of several isoforms of P-type ATPases (Toyoshima et al., 2004, 2007; Morth et al., 2007). A systematic comparison of XFs on SERCA (Danko et al., 2004) and their complex structures as determined by X-ray crystallography (Toyoshima et al., 2007; Olesen et al., 2007) suggested that the phosphate geometries mimicked by XFs were associated with specific conformational substates of the enzyme. When bound to the aspartyl residue in the P domain, the tetrahedral BeF stabilizes the E_2P "ground state", the trigonal bipyramidal AlF induces the E_2P^* "transition state", and the tetrahedral MgF induces the E_2P_i "product state" (Danko et al., 2004, see also Fig. 1). Furthermore, recent functional analyses regarding Ca^{2+}-induced reactivation of BeF-inhibited SERCA clearly illustrate the molecular mechanism upon reactivation (Danko et al., 2009). The binding of Ca^{2+} in the micromolar concentration range from the luminal Ca^{2+} binding site of SERCA E_2BeF induces the formation of an E_1P-like intermediate. Subsequent addition of Ca^{2+} in the millimolar concentration range to the cytoplasmic side is needed for the displacement of BeF at the phosphate binding site. However, extensive studies concerning the interaction of XFs with the H^+,K^+-ATPase remain sparse.

In order to understand conformational differences induced in the H^+,K^+-ATPase by each XF analog, we investigated their properties of inhibition, including stability and reversibility, and carried out structural analyses by employing electron crystallography of two-dimensional (2D) crystals. Although the structure of the BeF-inhibited H^+,K^+-ATPase was indistinguishable from the previously reported AlF-bound structure (Abe et al., 2009) at the currently achieved resolution level, our results clearly showed differences regarding the interaction of AlF and BeF with the H^+,K^+-ATPase.

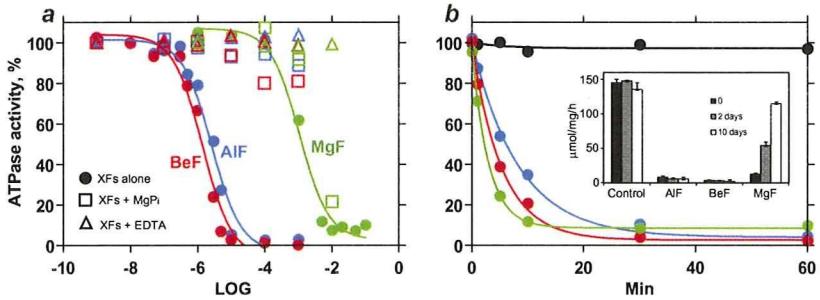

Fig. 2. Inhibition of H^+,K^+-ATPase activity by fluorinated phosphate analogs. (a) Dose-dependent inhibition of H^+,K^+-ATPase activity by XFs. SDS-purified membrane fractions (G2) were incubated at 37 °C for 1 h with indicated concentrations of AlF (blue symbols), BeF (red symbols) or MgF (green symbols), and ATPase activity was measured (filled circles and lines). Inhibition by XFs was also examined in the presence of MgP_i (open squares) and in the presence of EDTA but absence of $MgCl_2$ (open triangles). The values were plotted as a function of the logarithm of Al^{3+}, Be^{2+} and MgF concentrations, respectively. (b) Time course of inhibition by XFs. Membrane fractions were incubated without (control, black circles) or with 10 µM AlF (blue circles) or 10 µM BeF (red circles) or 10 mM MgF (green circles). At the indicated time, they were diluted 1000 times in sucrose buffer, and ATPase activity was measured. (Inset) Membrane fractions were treated with or without XFs indicated in the figure, and excess XF was removed by centrifugation. After suspending with sucrose buffer, they were stored at 3 °C, and their ATPase activities were measured at the indicated times (0–10 days).

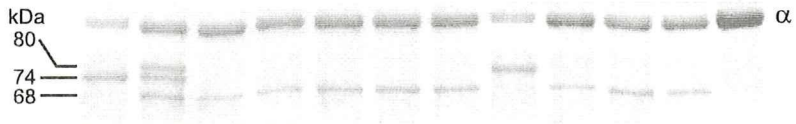

lane	1	2	3	4	5	6	7	8	9	10	11	12
Al^{3+}		0.2	0.1	1						5 mM MgATP	5 mM MgP_i	– trypsin
Be^{2+}					0.1	1	1					
F^-		0.8	1	4	1	4	4	1	10			
Mg^{2+}	0.1	0.1	0.1	0.1	0.1	0.1	0.1	0.1	10			
ADP		1					1					

Fig. 3. Limited trypsin digestion of XF-bound H^+,K^+-ATPases. Membrane fractions were incubated for 1 h at 37 °C in various conditions as indicated in the figure, followed by proteolysis by trypsin (see Section 2). The positions of the H^+,K^+-ATPase α-subunit (α) and its digestion fragments (80, 74 and 68 kDa) are indicated in the figure. See reference (Nishizawa et al., 2008) for detail.

2. Materials and methods

2.1. Preparation of H^+,K^+-ATPase-enriched membrane

H^+,K^+-ATPase-containing membrane fractions (G1, G2) were prepared, as described previously (Sachs et al., 1976) and further purified with SDS (Yen et al., 1990). These membrane fractions were stored at −80 °C in sucrose buffer (250 mM sucrose, 0.5 mM EGTA and 5 mM HEPES, pH 7.0) until use. Inhibition and reactivation measurements used a broken membrane preparation of the SDS-purified G2 fraction or G1 tight vesicles, in which H^+,K^+-ATPase was packed with the cytoplasmic side facing outwardly. For 2D crystallization, an SDS-purified G1 fraction was used, as described previously (Abe et al., 2009).

2.2. Inhibition of fluorinated complexes

For the inhibition of H^+,K^+-ATPase by XFs, membrane fractions (1 mg/ml) were incubated for 1 h at 37 °C in the presence of 40 mM HEPES/Tris, pH 7.0, 250 mM sucrose in the absence (control) or presence of 0.1 mM $AlCl_3$, 1 mM NaF, and 0.1 mM $MgCl_2$ (for AlF-inhibition) or 0.1 mM $BeSO_4$, 1 mM NaF, and 0.1 mM $MgCl_2$ (for BeF-inhibition) or 10 mM NaF and 10 mM $MgCl_2$ (for MgF-inhibition) followed by centrifugation to remove excess inhibitor. The resulting precipitates were suspended in sucrose buffer and used for the reactivation experiments. Inhibition by XFs was also examined in the presence of 10 mM $MgCl_2$ and 10 mM H_3PO_4 (MgP_i) and in the presence of 10 mM EDTA but absence of $MgCl_2$. The H^+,K^+-ATPase activity of the membrane fraction in the absence of XFs was set as 100%, and the specific H^+,K^+-ATPase inhibitor, SCH28080, (0.1 mM) was used for the blank values.

Reactivation was carried out with 1 mg/ml of control or XF-inhibited membrane fractions in the presence of 40 mM HEPES/Tris, pH 7.0 (MES buffer at pH 5.5 is used for "H^+" in the Fig. 3) and various cations (20 mM) as chloride salts, for 0–5 h at 37 °C. The samples were then 1000-fold diluted in sucrose buffer, and ATPase activities were measured colorimetrically (1.5 mM MgATP, 10 mM CH_3COOK, 250 mM sucrose, 40 mM HEPES/Tris, pH 7.0) according to (Chifflet et al., 1988).

For the measurement of dose-dependent inhibition by AlF or BeF (Fig. 2a), membrane fractions were incubated in the indicated concentrations of $AlCl_3$ (AlF) or $BeSO_4$ (BeF) in the presence of 1 mM NaF, 0.1 mM $MgCl_2$, 250 mM sucrose and 40 mM HEPES/Tris, pH 7.0. For MgF, an equal amount of $MgCl_2$ and NaF was used. After incubation for 1 h at 37 °C, membrane fractions were 1000-fold diluted, and the remaining ATPase activities were measured as described above. Notably, the presence of 1 mM NaF and 0.1 mM $MgCl_2$ alone, in the absence of Al^{3+} and Be^{2+}, did not inhibit H^+,K^+-ATPase activity.

2.3. Reactivation using tight vesicles

G1 fractions (1 mg/ml) were incubated for 1 h at 37 °C in the presence or absence of AlF, and tight vesicles were treated with or without 0.1% (w/v) escin to cause vesicles to leak. After washing these tight or leaky vesicles by centrifugation, reactivation was carried out in the presence of 250 mM sucrose, 40 mM HEPES/Tris, pH 7.0, with or without 5 mM $MgCl_2$. Samples were 1000-fold diluted in sucrose buffer in the presence or absence of the 1 μg/ml

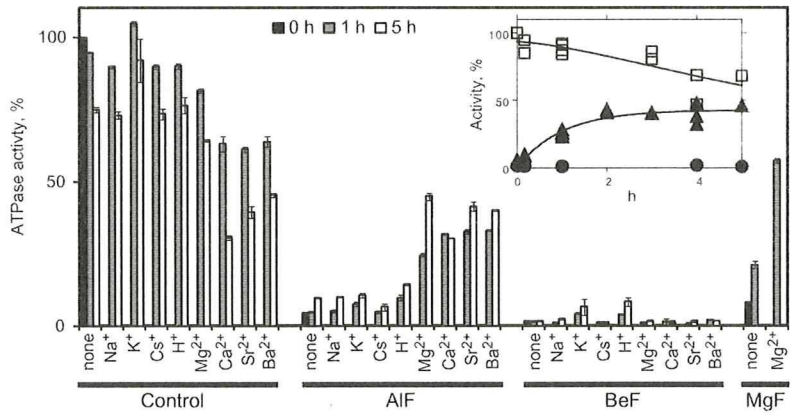

Fig. 4. Effect of various cations on XF-inhibited H^+,K^+-ATPase. Non-treated (control) or XF-treated SDS-purified membrane fractions (AlF, BeF and MgF) were incubated for 0 h (filled bars), 1 h (gray bars) and 5 h (open bars) at 37 °C with 20 mM of indicated cation as a chloride salt (20 mM MES, pH 5.5, is used for "H^+"). Specific ATPase activities were then determined. The inset shows the time course after addition of 20 mM $MgCl_2$ to the non-treated (open squares) or AlF-treated (closed triangles) or BeF-treated (closed circles) membrane fractions. The specific ATPase activity of the cation-free conditioned enzyme was defined as 100%.

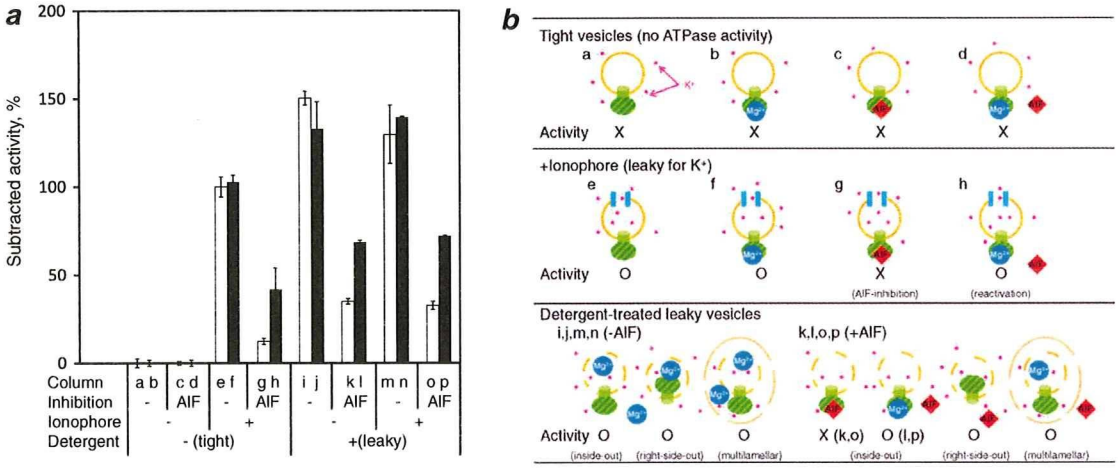

Fig. 5. Mg^{2+}-induced reactivation using inside-out tight vesicles. (a) G1 fractions were treated with or without AlF for 1 h at 37 °C ("tight" vesicle). After washing out excess AlF, samples were incubated for 1 h with (+Mg^{2+}, closed bars) or without (-Mg^{2+}, open bars) 5 mM Mg^{2+}. For "leaky" vesicles, 0.1% of escin was added at the time that the G1 fraction was treated with AlF. The ATPase activities of tight and leaky vesicles were then measured in the presence or absence of ionophore. See Section 2 for details. (b) Schematic drawing of the vesicles in each experimental condition (columns a-p in Fig. 5a). Yellow circles represent gastric vesicles, and green objects indicate H^+,K^+-ATPase molecules (shadowed oval area indicates cytoplasmic portion) embedded in the vesicles. Pink circles, blue circles, and red diamonds represent K^+, Mg^{2+} and AlF, respectively. Without ionophore (blue boxes) or detergent treatment (columns a–d, tight vesicles), H^+,K^+-ATPase showed no ATPase activity due to the lack of K^+ in the vesicles. When vesicles were treated with ionophore (columns e–h), H^+,K^+-ATPase in the inside-out vesicles exhibited full ATPase activity, except when inhibited by AlF (column g). The Mg^{2+}-induced reactivation of the AlF-inhibited enzyme (column h) indicated that Mg^{2+} was able to interact with the outside of the vesicles (namely, the cytoplasmic side of the enzyme). Note that right-side-out vesicles showed no ATPase activity when treated with ionophore, because ATP and Mg^{2+} could not pass through the membrane or ionophore. In the case of the detergent-treated vesicles (columns i–p), both ATP or Mg^{2+} diffused into the inside of permeabilized vesicles, therefore the large values of ATPase activities found in the detergent-treated vesicles suggested the presence of right-side-out or multilamellar vesicles. If the Mg^{2+}-induced reactivation had occurred from the luminal side of the enzyme, reactivation would be only observed in the detergent-treated vesicles (columns l, p), not in the ionophore-treated condition (column h). Since detergent treatment was performed just after AlF treatment (see Section 2), right-side-out or multilamellar vesicles were not inhibited by AlF and thus showed higher ATPase activities (columns k, l, o, p).

gramicidin, and their specific ATPase activities were determined. Note that the difference between ATPase activities with or without gramicidine indicates the amount of tight vesicles in the solution. Since the membrane preparation contained the same amount of leaky vesicles responsible for the background ATPase activity (100 ± 3 μmol/mg/h). The data shown in Fig. 5a represent activities after subtraction of these background values from the original data. Thus, the values presented in Fig. 5a were directly representative of the ATPase activities of tight vesicles. All values were normalized to the specific ATPase activity of gramicidine-treated tight vesicles in the absence of Mg^{2+} (Fig. 5a, column e, 123 ± 7 μmol/mg/h), which was set to 100%. Addition of Mg^{2+} induced around 40% reactivation of ATPase activity (Fig. 5a, column h), in agreement with the results obtained from broken membrane fractions (Fig. 4). Higher activities of escin-treated vesicles suggest the presence of a small amount of right-side-out and/or multilamellar vesicles.

2.4. Trypsin digestion

Limited proteolysis with trypsin using a purified G1 fraction was performed as described previously (Nishizawa et al., 2008). Before trypsin digestion, samples were incubated at the reaction conditions indicated in Fig. 3 for 1 h at 37 °C. Digestion was initiated by adding trypsin to the samples. The fragmented peptides were separated by SDS–PAGE using 10–20% polyacrylamide gradient gels (Supersep Ace, Wako, Japan).

2.5. 2D crystallization and image analysis

An SDS-purified G1 fraction (8 mg/ml of protein) was solubilized for 10 min on ice with 8 mg/ml octaethyleneglycol dodecylether ($C_{12}E_8$, Nikko chemical, Japan) in 40 mM MES, 20 mM $Mg(CH_3COO)_2$, 5 mM ATP, 10% (v/v) glycerol, 3 mM dithiothreitol (DTT), at pH 5.5 adjusted by Tris. After removal of the insoluble material by ultracentrifugation at 186,000*g* for 20 min, the supernatant was mixed with dioleoylphosphatidylcholine (Avanti) at a lipid-to-protein ratio (w/w) of 0.7–0.8. The samples were then placed in 10 μL microdialysis buttons (Hampton Research) using a dialysis membrane with a molecular weight cut-off of 25 kDa (SPECTRA/Pro #7, SPECTRUM), and first dialyzed against 10 mM MES, 10% (v/v) glycerol, 10 mM $MgCl_2$, 1 mM $BeSO_4$, 4 mM NaF, 1 mM ADP, 3 mM DTT, at pH 5.5 adjusted by Tris on ice for 1 day, and then against 20 mM propionate, 1 mM $MgCl_2$, 1 mM $BeSO_4$, 4 mM NaF, 1 mM ADP, 3 mM DTT, pH 4.8 with Tris at 3 °C for 12–16 days.

Samples were negatively stained with 2% (w/v) uranyl acetate to screen for crystallization conditions. Sample preparations for cryo-electron microscopy and image processing were as described previously (Abe et al., 2009). Briefly, specimens were prepared in the cold room using the carbon sandwich method (Gyobu et al., 2004). Images were recorded with a JEM-3000SFF electron microscope (JEOL) equipped with a super fluid helium stage (Fujiyoshi et al., 1991; Fujiyoshi, 1998) on SO-163 films (Kodak). Digitized images were processed with the MRC image processing programs (Crowther et al., 1996) and their initial contrast transfer function parameters were determined (Tani et al., 1996) for correction. The data tilted to 45° were merged using LATLINE (Agard, 1983) and used to calculate a 3D density map at 8 Å resolution (Table S1). The density responsible for the αβ-protomer was extracted using the program CODIV (Volkmann, 2002). Figures were prepared using Pymol (http://pymol.sourceforge.net/).

3. Results

3.1. Inhibition of H^+,K^+-ATPase activities by fluorinated complexes

The ability of XFs to inhibit the H^+,K^+-ATPase by acting as phosphate analogs was investigated. The results showed a rapid and dose-dependent inhibition of H^+,K^+-ATPase activity (Fig. 2a and b),

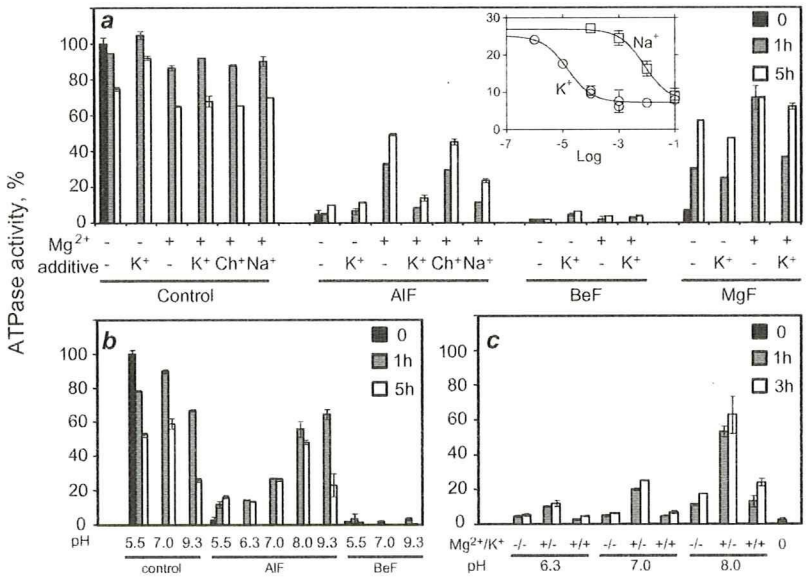

Fig. 6. Effects of transported cations and Mg^{2+} on XF-inhibited H^+,K^+-ATPase. (a) ATPase activity of SDS-treated XF-inhibited G2 fractions after incubation for 1 h (closed column) or 5 h (open column) at 37 °C in the presence or absence of 20 mM $MgCl_2$ and other cations, as indicated. (Inset) dose-dependence of the K^+-dependent suppression of Mg^{2+}-induced reactivation. AlF-inhibited enzymes were incubated for 1 h at 37 °C in 20 mM $MgCl_2$ and the indicated concentrations of KCl (circles) or NaCl (squares) at pH 7.0. (b) Mg^{2+}-induced reactivation at different pHs. Non-treated (control, filled bars) or AlF- or BeF-inhibited preparations were incubated for 1 h (gray bars) or 5 h (open bars) at 37 °C in the presence of 20 mM $MgCl_2$, and 20 mM buffer (MES for pH 5.5 or 6.3, HEPES for pH 7.0, Tris for pH 8.0 or 9.3; all buffers adjusted with Tris or HCl), then ATPase activity was measured at pH 7.0. (c) Mg^{2+}-induced reactivation of AlF-inhibited enzyme and its suppression by K^+ at different pHs. An AlF-inhibited preparation was incubated at 37 °C for 1 h (gray bars) or 3 h (open bars) at the indicated pH (as in b) with or without 20 mM $MgCl_2$ and/or KCl. Filled bars indicate ATPase activities without incubation (time zero). All values were normalized to the activity of untreated H^+,K^+-ATPase as 100%.

similar to the effects seen on SERCA. Whereas both, AlF and BeF, clearly showed a high affinity (IC_{50} = 2.6 μM and 1.4 μM for added $AlCl_3$ and $BeSO_4$, respectively), a much higher concentration was required in the case of MgF (IC_{50} = 1.1 mM) to inhibit the enzyme activity. Inhibition of H^+,K^+-ATPase activity by AlF or BeF appeared to be stable for more than 1 week at 4 °C after washing out free XFs, but MgF inhibition was less stable than the others (Fig. 2b, inset). However, the inhibition by each XF was significantly reduced by the presence of Mg^{2+} and inorganic phosphate (MgP_i) or EDTA (Fig. 2a, open squares or triangles, respectively), indicating that the inhibition by all XFs is competitive to inorganic phosphate and depends on Mg^{2+}. Since the formation of the aspartylphosphate from either ATP or P_i requires Mg^{2+}, the aforementioned results suggest that all XFs mimic the bound phosphate with a coordinating Mg^{2+} ion.

To reveal the conformational state of the XF-inhibited H^+,K^+-ATPase, limited trypsin cleavage (Fig. 3) was applied to the XF-bound enzyme. As reported previously (Nishizawa et al., 2008), addition of AlF with ADP induces a digestion pattern which corresponds to the E_1P-ADP intermediate (lane 2), whereas AlF alone (lane 4), BeF in the absence (lanes 5 and 6) or in the presence of ADP (lane 7, same conditions used for the 2D crystallization described below), and high concentrations of Mg^{2+} and F^- (lane 9) yielded peptide patterns similar to those found in E_2P state (lane 10, MgATP or lane 11, MgP_i). These data led us to conclude that all XF-inhibited enzymes represent an E_2P-like conformation. It is notable that low concentrations of Mg^{2+} and F^- (lane 8) result in a fragment pattern identical to E_1 (lane 1, in the absence of ligands). This suggests that Mg^{2+} and F^- at low concentrations, which would be sufficient for the inhibition in case of AlF and BeF, has negligible effects on either enzyme conformation or ATPase activity (Fig. 2a).

3.2. Reactivation of AlF-inhibited H^+,K^+-ATPase by divalent cations

A systematic comparison of the effects of XFs on SERCA has shown that the activity of the BeF-inhibited ATPase could be rapidly restored by Ca^{2+} from the luminal side, but neither the AlF- nor the MgF-inhibited enzyme could be reactivated (Danko et al., 2004). We therefore examined the reactivation properties of XF-inhibited H^+,K^+-ATPase with various cations (Fig. 4). Unlike SERCA, reactivation was not achieved in BeF-inhibited H^+,K^+-ATPase with any of examined cations, and also not at low pH. The AlF-inhibited H^+,K^+-ATPase, however, could largely be reactivated by the addition of any divalent cation, although the activity of the control enzyme decreased gradually, probably due to aggregate formation (inset of Fig. 4, open squares). Inhibition by MgF is reversible during long-term storage at 3 °C (Fig. 2b, inset), and this process is substantially accelerated by incubation at 37 °C without addition of any divalent cations (Fig. 4).

In order to identify from which side of the membrane the reactivation occurs, we studied reactivation using inside-out tight vesicles (see Section 2 for details). Since the vesicles are prepared from the parietal cells of pig gastric mucosa (Sachs et al., 1976), the light membrane fraction (G1) predominantly contains tightly sealed inside-out tubular vesicles, in which H^+,K^+-ATPase molecules expose their cytoplasmic side to the outside. In these tight vesicles, H^+,K^+-ATPase shows little ATPase activity when K^+ is absent in the vesicle lumen. Addition of the K^+ ionophore gramicidine (note that this ionophore permeates only monovalent cations, but not divalent cations such as Mg^{2+}) or treatment with the mild detergent escin induces the leakage of the tight vesicles, resulting in full ATPase activity (Fig. 5a). Therefore, the almost doubled ATPase activity of the ionophore-treated vesicles compared with non-treated tight vesicles (223 μmol/mg/h versus 100 μmol/mg/h in the absence of ionophore) suggests that more than 50% of the vesicles were tightly sealed from the outside solution. The much higher ATPase activity of detergent-treated vesicles is attributable to the contamination of right-side-out and/or multilamellar vesicles (Fig. 5b).

The enzyme activity in the tight vesicle fraction was also inhibited by the bulk AlF solution and partially restored by addition of Mg^{2+} (Fig. 5), similar to the results using broken membrane

fractions (Fig. 2). Since in the tight vesicles only the cytoplasmic side of the enzyme is accessible, the increased ATPase activity of Mg^{2+}-reactivated tight vesicles permeabilized by the ionophore suggests that Mg^{2+}-reactivation is taking place on the cytoplasmic side (see Fig. 5 and its legend for details). Even if H^+,K^+-ATPase molecules in the tight vesicles were reactivated by Mg^{2+}, they could not exhibit ATPase activity without K^+ at the luminal side of the membrane which, in this case, was supplied by permeabilizing the tight vesicles with either a ionophore or detergent (Fig. 5b). Furthermore, since the detergent-treated vesicles (Fig. 5a, columns l–k or p–o) do not show an increased amount of reactivation compared with the ionophore-treated ones (Fig. 5a, columns h–g), an additional reactivating effect by luminal Mg^{2+} can be excluded.

3.3. Prevention of the Mg^{2+}-induced reactivation by K^+ binding

Based on the previously reported Ca^{2+}-induced reactivation mechanism for SERCA (Danko et al., 2004), the effects of the transported cations on the H^+,K^+-ATPase was examined. The results clearly showed that the Mg^{2+}-induced reactivation of the AlF-inhibited enzyme was strongly suppressed in the presence of K^+ (Fig. 6a). The high affinity ($K_{0.5}$ = 15 μM) of K^+ for suppression (Fig. 6a, inset) suggested that the binding of K^+ is specific and might occur at the TM cation binding site. Furthermore, the negligible effect of choline (Ch^+) chloride on the Mg^{2+}-induced reactivation also excludes a non-specific effect of ion strength. It is notable, however, that 20 mM Na^+ also suppresses Mg^{2+}-induced reactivation (Fig. 6a, inset). Since high concentrations of Na^+ have been shown to compete with either cytoplasmic H^+ or luminal K^+ (Rabon and Reuben, 1990), Na^+ partially mimics the K^+ effect, albeit with a much lower affinity ($K_{0.5}$ = 8 mM) (Fig. 6a, inset). The results presented above suggest that K^+ can access the cation binding site(s) in the E_2AlF state, and stabilizes its whole conformation against Mg^{2+}-reactivation.

Considering the reactivation of BeF-inhibited SERCA by luminal Ca^{2+} (Danko et al., 2009), it seems possible that acidic pH could induce a transition from the E_2BeF state of the H^+,K^+-ATPase toward an E_1P-like conformation, in which bound BeF may be exchangeable with a divalent cation. Therefore, we employed buffer solutions with various pH values to clarify the impact of H^+ on Mg^{2+}-induced reactivation. The results of AlF-inhibited enzyme showed that the magnitude of the Mg^{2+}-induced reactivation was highly pH dependent, whereas the BeF-inhibited enzyme was not affected (Fig. 6b). At basic pH, Mg^{2+}-induced reactivation of AlF-inhibited enzyme was enhanced regardless of Mg^{2+} concentration (Fig. 6c). Furthermore, suppressive action by K^+ was observed at every pH tested for AlF-inhibited enzyme (Fig. 6c). Since the H^+,K^+-ATPase appears to be stabilized in the E_2P state by interactions with the β-subunit thereby prohibiting the physiologically unfavorable reverse reaction (Dürr et al., 2008, 2009; Abe et al., 2009), most of the H^+,K^+-ATPase molecules are accumulated in the E_2P state in this pH range (pH 5.5–9.3) (Helmich-de Jong et al., 1985). Therefore, the pH conditions applied here may not be sufficient to shift E_2BeF H^+,K^+-ATPase into an E_1P-like conformation.

3.4. Cryo-EM structure of BeF-bound H^+,K^+-ATPase

In order to understand the distinct properties of XFs when bound to the H^+,K^+-ATPase, we attempted to solve the three-dimensional structure of BeF-bound H^+,K^+-ATPase employing electron crystallography of two-dimensional (2D) crystals and to compare it to the previously reported E_2AlF structure (Abe et al., 2009). However, we have so far failed to produce 2D crystals of the MgF-bound form of sufficient quality for the structural analysis, probably due to the weak and partial inhibition observed in the reactivation experiments (Figs. 2, 4 and 6).

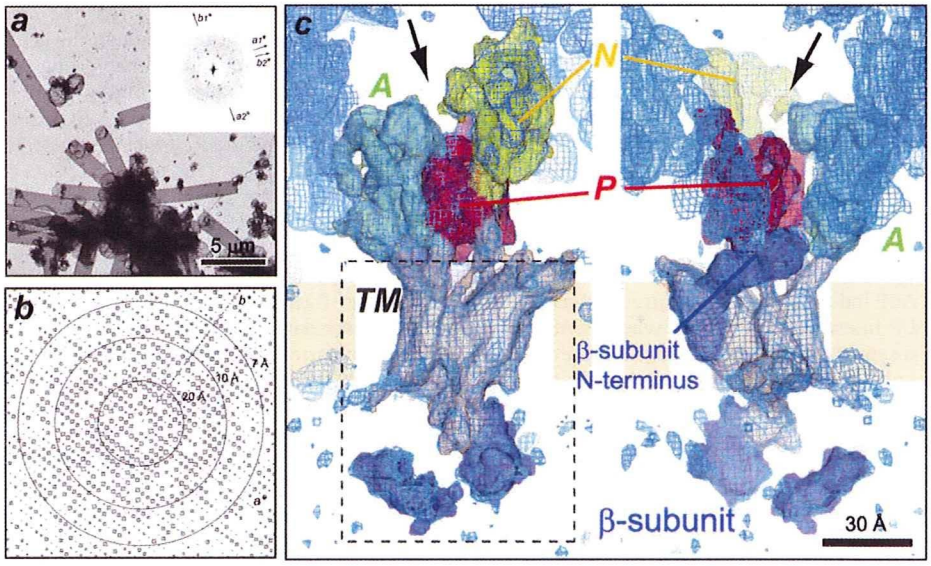

Fig. 7. Cryo-EM structure of BeF-bound H^+,K^+-ATPase at 8 Å resolution. (a) Negatively stained thick tubular crystals. (Inset) Fourier transform of negatively stained 2D crystal shows two overlapped lattices ($a_1^*b_1^*$ and $a_2^*b_2^*$). (b) IQ-plot (Henderson et al., 1986) calculated from Fourier transform of the frozen-hydrated 2D crystal. Circles indicate 1/20, 1/10 and 1/7 $Å^{-1}$, respectively. (c) Three-dimensional structure of the BeF-bound H^+,K^+-ATPase (blue mesh, contoured 1.0 σ) with the superimposed AlF-bound EM structure [surface, EMDB (http://www.ebi.ac.uk/msd-srv/emserch/index.html), accession number 5104, see Abe et al., 2009 for detail]. Surface color code of the density map: N domain, yellow; P domain, red; A domain, green; TM domain of the α-subunit, wheat; β-subunit, blue. The boxed region with the dashed line corresponds to the view in Fig. 7a, and a black arrow in both panels indicates the position from the same viewpoint as Fig. 7b. Left and right panels are related to the 180° rotation along the axis perpendicular to the membrane plane. An αβ-protomer is displayed with cytoplasmic side up. Please note that the excess volume of blue mesh is due to other protomers related by crystallographic $p22_12_1$ symmetry. Scale bar, 30 Å.

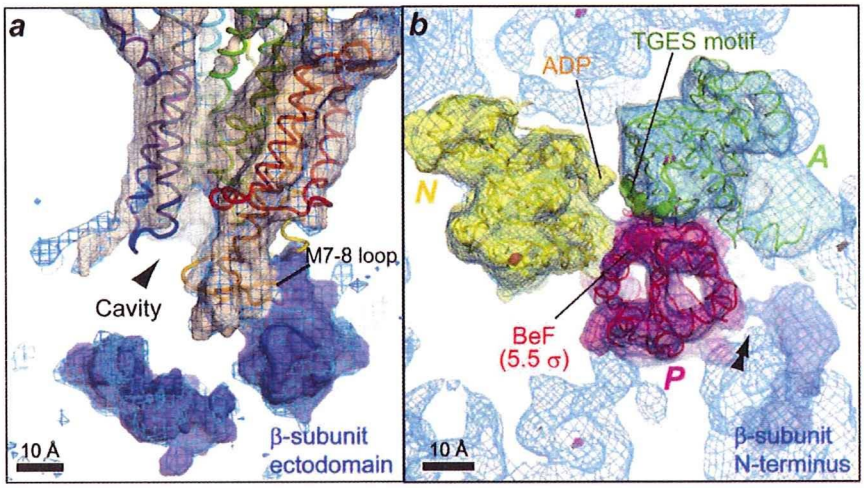

Fig. 8. Structural comparison of H^+,K^+-ATPase in the E_2BeF and E_2AlF states. E_2BeF (blue mesh) and E_2AlF (surface, color codes as in Fig. 6c) structures of H^+,K^+-ATPase are superimposed with a homology model of H^+,K^+-ATPase E_2AlF state (PDB ID 3IXZ, color code: A, N and P domains, same color as the density map; TM helices, gradually change from M1 (blue) to M10 (red)). (a) Magnified view of the cavity structure (arrowhead) at the luminal side of the TM domain (the same boxed region in Fig. 6c). (b) Conformation of the cytoplasmic domains viewed from the direction indicated in Fig. 6c. Double arrowhead indicates an interface between the P domain and the β-subunit *N*-terminus. The invariant ^{228}TGES motif, which is important for the dephosphorylation, is highlighted with its main chain depicted as a green sphere model. A strong density (contoured above 5.5 σ, red sphere) found in the middle of the P domain most likely represents a bound BeF complex. Scale bars, 10 Å.

Thick tubular crystals were grown in the presence of BeF (Fig. 7a), thus two crystalline layers always overlapped in the projection images (Fig. 7a, inset). Therefore, the 2D crystals in the upper and the lower layer of the flattened tubes were processed individually by indexing each lattice separately (Fig. 7b), and processed images tilted to an angle of 45° were merged. The final 3D density map was calculated to 8 Å resolution (Fig. 7c, Table S1). Like the previously reported AlF-bound 2D crystal (Abe et al., 2009), one crystalline layer consists of two membrane layers (not shown). The asymmetric unit contains one H^+,K^+-ATPase αβ-protomer, and the αβ-protomers are related to each other by a crystallographic 2-fold screw axis.

The X-ray structures of E_2BeF SERCA have revealed specific conformations, notably the opening of the luminal gate (Olesen et al., 2007, PDB code 3B9B), and the orientation of the A domain and the connecting M2 helix (Toyoshima et al., 2007, PDB code 2ZBE), which are distinct from the E_2AlF transition state (PDB code 3B9R). The present cryo-EM structure of E_2BeF H^+,K^+-ATPase is, however, nearly identical to that of the E_2AlF state (Abe et al., 2009, EMDB # 5104), including the cavity structure of the TM domain (Fig. 8a), the XF binding site at the P domain, and the relative orientation of the cytoplasmic domains (Fig. 8b). Since bound phosphate analogs are hardly exposed to the solution (Fig. 8b), the conformational difference between the E_2AlF and E_2BeF structures is unlikely to reveal any distinctive feature concerning the Mg^{2+}-induced reactivation process. Therefore, the stability of the spatial arrangement of the cytoplasmic domains, which would be directly related to the coordination of respective phosphate analogs, may entail their characteristic reactivation properties, as discussed below.

4. Discussion

4.1. Possible mechanisms for the reactivation of AlF-inhibited H^+,K^+-ATPase

Our experimental data clearly showed that the reactivation is induced in the "*E_2P-like*" conformation (Fig. 3) of either "*AlF*"- or "*MgF*"-inhibited H^+,K^+-ATPase by the addition of "*divalent cations*" (Fig. 4) from the "*cytoplasmic side*" (Fig. 5). Although the observed phenomena are similar, the properties of reactivation are clearly different from SERCA, in which the "*BeF*"-bound form can be reactivated by "Ca^{2+}" from the "*luminal side*" (Danko et al., 2004). In the case of SERCA, the displacement of BeF by cytoplasmic Ca^{2+} occurs in the "*E_1P-like*" conformation, which is induced by the binding of Ca^{2+} from the luminal side of E_2BeF state (Danko et al., 2009). It is also notable that the high concentration of Mg^{2+} or Ca^{2+} did not induce the reactivation of XF-inhibited SERCA in the E_2P-like conformation. (T. Daiho, personal communication). Therefore, as observed in the X-ray structures of SERCA, both AlF and BeF are isolated from the bulk solution by the P domain and the highly conserved TGES-loop of the A domain, thus divalent cations cannot access the bound phosphate analogs in the SERCA E_2AlF or E_2BeF states.

In our EM map of the H^+,K^+-ATPase in the E_2AlF or E_2BeF states, bound AlF or BeF do not appear to be exposed to the bulk solution (Fig. 8b). Therefore, we attempted to correlate the differences in the observed reactivation properties of XFs with the conformational stabilities caused by their different coordination effects of the surrounding P domain and TGES-loop. Although the coordination of AlF or MgF by the A and P domains appears to be less tight than that of BeF in the X-ray structures of SERCA, all bound XFs are inaccessible from the bulk solution (Olesen et al., 2007; Toyoshima et al., 2007). The cytoplasmic domains of the H^+,K^+-ATPase create a similarly shielded conformation around the phosphate analogs, making it likely that the replacement of AlF by divalent cations would be difficult. Because the amino acid residues involved in the coordination of the phosphate analogs are well-conserved between H^+,K^+-ATPase and SERCA, the different reactivation property is likely independent of the XF's structure in the P domains themselves. However, a potentially important structural difference was found in the cytoplasmic region. In the case of H^+,K^+-ATPase (Fig. 9, mesh representation) and the closely related Na^+,K^+-ATPase (Shinoda et al., 2009), the N domain hardly interacts with the A domain, although three cytoplasmic domains form a compact configuration with an intimate contact between the A and N domain in E_2BeF SERCA structure (Fig. 9, surface representation). We therefore propose that the relative flexibility of the A domain of H^+,K^+-ATPase caused by the lack of interaction between the A and N domains (arrow in Fig. 9) increases the likelihood of AlF-

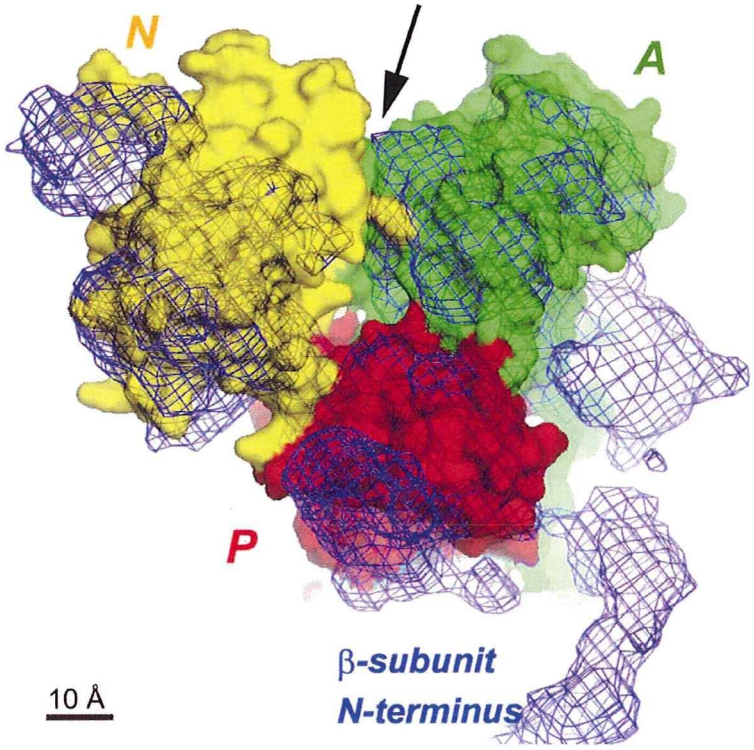

Fig. 9. Comparison of the H^+,K^+-ATPase with SERCA in the E_2AlF state. The crystal structure of SERCA with E_2AlF (PDB ID 3R9B, color code: A domain, green; P domain, red; N domain, yellow) was fitted into the cryo-EM map of H^+,K^+-ATPase with E_2AlF-ADP (blue mesh, EMBD 5104). The figure was drawn from the same viewpoint as in Fig. 7B. A black arrow indicates intimate interaction between the A and N domain of SERCA. By contrast, these two domains are separated in the H^+,K^+-ATPase structure. Scale bar, 10 Å.

exposure to the bulk solution by thermal fluctuations of the A and/or P domain. Because the coordination chemistry of BeF is strikingly similar to the phosphate group (Petsko, 2000) and because of its high charge density due to its small size, BeF may provide a more stable conformation than AlF or MgF. Unfortunately, extensive studies concerning the interaction of XFs with the Na^+,K^+-ATPase are missing. However, the similar orientations of the cytoplasmic domains of H^+,K^+- and Na^+,K^+-ATPase might entail similar properties regarding the inhibition by XFs.

Our results also suggest that both AlF-inhibition and partial MgF-inhibition are stabilized by K^+ binding at the TM cation binding site (Fig. 6a). This stabilization effect of K^+ indicates that the K^+ binding site is accessible in the E_2AlF state, although the luminal cavity seems not to extend to the cation binding site in the E_2AlF H^+,K^+-ATPase structure without K^+ (Abe et al., 2009). Therefore, we propose that thermal fluctuations at the TM domain, together with the mobility of the cytoplasmic domains, could induce a short-time exposure of the luminal K^+ binding site. This might be also related to the role of the β-subunit which stabilized K^+-occluded conformation of Na^+,K^+-ATPase (Lutsenko and Kaplan, 1993).

4.2. Implications of the structural and functional difference between H^+,K^+-ATPase and SERCA

Comparison of SERCA structures in the E_2AlF and E_2BeF states revealed a significant difference regarding the luminal gating, which was open in the BeF- and closed in the AlF-structure (Toyoshima et al., 2007; Olesen et al., 2007). In the EM structures of the E_2AlF and the E_2BeF H^+,K^+-ATPase, neither the luminal gate nor the location of cytoplasmic domains show significant differences (Figs. 7c and 8). Here, we propose several possible reasons why H^+,K^+-ATPase undergoes a different conformational transition than SERCA upon addition of AlF or BeF, as follows: (1) A widely opened luminal gate is not necessary for releasing H^+ to the luminal side, since the transfer of H^+ could proceed according to the Grotthuss mechanism (Karjalainen et al., 2007). (2) Such a luminal-facing conformation might be short-lived because of the highly acidic conditions in the luminal solution *in vivo*. (3) To reduce the risk of H^+ reverse flow, H^+,K^+-ATPase might prefer the E_2P transition state rather than the E_2P ground state in which luminal H^+ can bind and reverse the cycle into E_1P. According to our EM structures large conformational changes between E_2BeF and E_2AlF states are unlikely, however, subtle changes cannot be excluded. High-resolution structures of H^+,K^+-ATPase with XFs should therefore be determined to further understand the molecular mechanism of H^+ release and K^+ entrance in the E_2P state.

Each isoform of the P-type ATPase forms a unique cation gradient in each cell and organelle that express it; *i.e.* the H^+,K^+-ATPase generates a million-fold H^+ gradient across the gastric membrane, the SERCA pumps Ca^{2+} into SR vesicles to keep a low Ca^{2+} concentration in the cytoplasm for proper muscle contraction as well as survival of cells, and the Na^+,K^+-ATPase produces the primary Na^+ and K^+ gradients which are indispensable for secondary transport and action potential generation in nerve cells. Therefore, the different conformations induced by BeF in the H^+,K^+-ATPase and SERCA may imply that the energetically most favored conformation is different among P-type ATPases in order to fulfill their unique role in producing a suitable environment *in vivo*.

Acknowledgments

We thank Mr. K. Kobayashi (JEOL DATUM) for technical assistance with electron microscopy. We are grateful to Drs. T. Daiho, H.

Suzuki, C. Gerle and K. Taniguchi for valuable discussion. We also appreciate Drs T. Friedrich and K. Dürr for their helpful comments and critical reading of this manuscript. This research was supported by Grants-in-Aid for Specially Promoted Research, the Grobal COE Program A06 to Kyoto University, and the Japan New Energy and Industrial Technology Development Organization (NEDO).

Appendix A. Supplementary data

Supplementary data associated with this article can be found, in the online version, at doi:10.1016/j.jsb.2009.12.008.

References

Abe, K., Tani, K., Nishizawa, T., Fujiyoshi, Y., 2009. Inter-subunit interaction of gastric H^+,K^+-ATPase prevents reverse reaction of the transport cycle. EMBO J. 28, 1637–1643.

Agard, D.A., 1983. A least-squares method for determining structure factors in three-dimensional tilted-view reconstructions. J. Mol. Biol. 167, 849–852.

Bigay, J., Deterre, P., Pfister, C., Chabre, M., 1987. Fluoride complexes of aluminium or beryllium act on G-proteins as reversibly bound analogues of the gamma phosphate of GTP. EMBO J. 6, 2907–2913.

Chifflet, S., Torriglia, A., Chiesa, R., Tolosa, S., 1988. A method for the determination of inorganic phosphate in the presence of labile organic phosphate and high concentrations of protein: application to lens ATPases. Anal. Biochem. 168, 1–4.

Chow, D.C., Forte, J.G., 1995. Functional significance of the beta-subunit for heterodimeric P-type ATPases. J. Exp. Biol. 198, 1–17.

Crowther, R.A., Henderson, R., Smith, J.M., 1996. MRC image processing programs. J. Struct. Biol. 116, 9–16.

Danko, S., Yamasaki, K., Daiho, T., Suzuki, H., 2004. Distinct natures of beryllium fluoride-bound, aluminum fluoride-bound, and magnesium fluoride-bound stable analogues of an ADP-insensitive phosphoenzyme intermediate of sarcoplasmic reticulum Ca^{2+}-ATPase: changes in catalytic and transport sites during phosphoenzyme hydrolysis. J. Biol. Chem. 279, 14991–14998.

Danko, S., Daiho, T., Yamasaki, K., Liu, X., Suzuki, H., 2009. Formation of stable structural analog of ADP-sensitive phosphoenzyme of Ca^{2+}-ATPase with occluded Ca^{2+} by beryllium fluoride: structural changes during phosphorylation and isomerization. J. Biol. Chem. 284, 22722–22735.

Dürr, K.L., Tavraz, N.N., Dempski, R.E., Bamberg, E., Friedrich, T., 2008. Functional significance of E_2 state stabilization by specific alpha/beta-subunit interactions of Na,K- and H,K-ATPase. J. Biol. Chem. 284, 3842–3854.

Dürr, K.L., Abe, K., Tavraz, N.N., Friedrich, T., 2009. E2P-state stabilization by the *N*-terminal tail of the H,K-ATPase β-subunit is critical for efficient proton pumping under in vivo conditions. J. Biol. Chem. 284, 20147–20154.

Fujiyoshi, Y., 1998. The structural study of membrane proteins by electron crystallography. Adv. Biophys. 35, 25–80.

Fujiyoshi, Y., Mizusaki, T., Morikawa, K., Yamagishi, H., Aoki, Y., Kihara, H., Harada, Y., 1991. Development of a superfluid helium stage for high-resolution electron microscopy. Ultramicroscopy 38, 241–251.

Ganser, A.L., Forte, J.G., 1973. K^+-stimulated ATPase in purified microsomes of bullfrog oxynic cells. Biochim. Biophys. Acta 307, 169–180.

Gyobu, N., Tani, K., Hiroaki, Y., Kamegawa, A., Mitsuoka, K., Fujiyoshi, Y., 2004. Improved specimen preparation for cryo-electron microscopy using a symmetric carbon sandwich technique. J. Struct. Biol. 146, 325–333.

Helmich-de Jong, M.L., van Emst-de Vries, S.E., De Pont, J.J., Schuurmans Stekhoven, F.M., Bonting, S.L., 1985. Direct evidence for an ADP-sensitive phosphointermadiate of ($K^+ + H^+$)-ATPase. Biochim. Biophys. Acta 821, 377–383.

Henderson, R., Baldwin, J., Downing, K., Lepault, J., Zemiln, F., 1986. Structure of purple membrane from *Halobacterium halobium*: recording, measurement and evaluation of electron micrographs at 3.5 Å resolution. Ultramicroscopy 19, 147–178.

Karjalainen, E.-L., Hauser, K., Barth, A., 2007. Proton paths in the sarcoplasmic reticulum Ca^{2+}-ATPase. Biochim. Biophys. Acta 1767, 1310–1318.

Lutsenko, S., Kaplan, J.H., 1993. An essential role for the extracellular domain of the sodium–potassium-ATPase β-subunit in cation occlusion. Biochemistry 32, 6737–6743.

Morth, J.P., Poulsen, H., Toustrup-Jensen, M.S., Schack, V.R., Egebjerg, J., Andersen, J.P., Vilsen, B., Nissen, P., 2007. Crystal structure of the sodium–potassium pump. Nature 450, 1043–1049.

Nishizawa, T., Abe, K., Tani, K., Fujiyoshi, Y., 2008. Structural analysis of 2D crystals of gastric H^+,K^+-ATPase in different states of the transport cycle. J. Struct. Biol. 162, 219–228.

Olesen, C., Picard, M., Winther, A.M., Gyrup, C., Morth, J.P., Oxvig, C., Møller, J.V., Nissen, P., 2007. The structural basis of calcium transport by the calcium pump. Nature 450, 1036–1042.

Palmgren, M.G., Axelsen, K.B., 1998. Evolution of P-type ATPases. Biochim. Biophys. Acta 1365, 37–45.

Petsko, G.A., 2000. Chemistry and biology. Proc. Natl. Acad. Sci. USA 97, 538–590.

Post, R.L., Kume, S., 1973. Evidence for an aspartyl phosphate residue at the active site of sodium and potassium ion transport adenosine triphosphatase. J. Biol. Chem. 248, 6993–7000.

Rabon, E.C., Reuben, M.A., 1990. The mechanism and structure of the gastric H,K-ATPase. Annu. Rev. Physiol. 52, 321–344.

Sachs, G., Chang, H.H., Rabon, E., Schackman, R., Lewin, M., Saccomani, G., 1976. A nonelectrogenic H^+ pump in plasma membrane of hog stomach. J. Biol. Chem. 251, 7690–7698.

Sachs, G., Shin, J.M., Vagin, O., Lambrecht, N., Yakubov, I., Munson, K., 2007. The gastric H,K ATPase as a drug target past, present, and future. J. Clin. Gastroenterol. 41, S226–S242.

Shinoda, T., Ogawa, H., Cornelius, F., Toyoshima, C., 2009. Crystal structure of the sodium–potassium pump at 2.4 Å resolution. Nature 459, 446–450.

Tani, K., Sasabe, H., Toyoshima, C., 1996. A set of computer programs for determining defocus and astigmatism in electron images. Ultramicroscopy 65, 31–44.

Toyoshima, C., Nomura, H., Tsuda, T., 2004. Luminal gating mechanism revealed in calcium pump crystal structures with phosphate analogues. Nature 432, 361–368.

Toyoshima, C., Norimatsu, Y., Iwasawa, S., Tsuda, T., Ogawa, H., 2007. How processing of aspartylphosphate is coupled to luminal gating of the ion pathway in the calcium pump. Proc. Nat. Acad. Sci. USA 104, 19831–19836.

Volkmann, N.A., 2002. Novel three-dimensional variant of the watershed transform for segmentation of electron density maps. J. Struct. Biol. 138, 123–129.

Wolosin, J.M., 1985. Ion transport studies with H^+-K^+-ATPase-rich vesicles: implications for HCl secretion and parietal cell physiology. Am. J. Physiol. 248, G595–G607.

Yen, L.A., Cosgrove, P., Holt, W., 1990. SDS purification of porcine H,K-ATPase from gastric mucosa. Membr. Biochem. 9, 129–140.

THE JOURNAL OF BIOLOGICAL CHEMISTRY VOL. 285, NO. 6, pp. 3685–3694, February 5, 2010

Comparative Study of the Gating Motif and C-type Inactivation in Prokaryotic Voltage-gated Sodium Channels*

Received for publication, September 10, 2009, and in revised form, December 2, 2009 Published, JBC Papers in Press, December 3, 2009, DOI 10.1074/jbc.M109.057455

Katsumasa Irie[‡§], Kazuya Kitagawa[‡], Hitoshi Nagura[‡1], Tomoya Imai[¶], Takushi Shimomura[‡], and Yoshinori Fujiyoshi[‡2]

From the [‡]Department of Biophysics, Graduate School of Science, Kyoto University, Oiwake, Kitashirakawa, Sakyo-ku, Kyoto 606-8502, the [§]Japan Biological Informatics Consortium, Oiwake, Kitashirakawa, Sakyo-ku, Kyoto 606-8502, and the [¶]Research Institute for Sustainable Humanosphere (RISH), Kyoto University, Gokasho, Uji, Kyoto 611-0011, Japan

Prokaryotic voltage-gated sodium channels (Na_Vs) are homotetramers and are thought to inactivate through a single mechanism, named C-type inactivation. Here we report the voltage dependence and inactivation rate of the NaChBac channel from *Bacillus halodurans*, the first identified prokaryotic Na_V, as well as of three new homologues cloned from *Bacillus licheniformis* (Na_VBacL), *Shewanella putrefaciens* (Na_VSheP), and *Roseobacter denitrificans* (Na_VRosD). We found that, although activated by a lower membrane potential, Na_VBacL inactivates as slowly as NaChBac. Na_VSheP and Na_VRosD inactivate faster than NaChBac. Mutational analysis of helix S6 showed that residues corresponding to the "glycine hinge" and "PXP motif" in voltage-gated potassium channels are not obligatory for channel gating in these prokaryotic Na_Vs, but mutations in the regions changed the inactivation rates. Mutation of the region corresponding to the glycine hinge in Na_VBacL (A214G), Na_VSheP (A216G), and NaChBac (G219A) accelerated inactivation in these channels, whereas mutation of glycine to alanine in the lower part of helix S6 in NaChBac (G229A), Na_VBacL (G224A), and Na_VRosD (G217A) reduced the inactivation rate. These results imply that activation gating in prokaryotic Na_Vs does not require gating motifs and that the residues of helix S6 affect C-type inactivation rates in these channels.

Voltage-gated sodium channels (Na_Vs)[3] generate the rapid upstroke of action potentials in nerve cell axons (1). In mammalian Na_Vs, the channel is formed by the α-subunit, which comprises four repeats of six-transmembrane segments, with each repeat consisting of 300–400 amino acids. The α-subunit carries several glycosylation sites and co-assembles with auxiliary subunits to form the native channel (2, 3). The only structural information on Na_Vs available to date is a density map of the Na_V from the electric organ of the electric eel determined by cryoelectron microscopy (4). Due to its limited resolution of 19 Å, the density map did not provide insights into the gating or sodium selectivity.

The first prokaryotic Na_V, NaChBac, was cloned from *Bacillus halodurans* (5). Subsequently, three more prokaryotic sodium channels were cloned and characterized (6, 7). All studied prokaryotic Na_Vs form homotetramers with a structure thought to be similar to that of some potassium channels with known structures (8–10). Furthermore, because the proteins could be expressed in large amounts in *Escherichia coli* and purified by metal chelate affinity chromatography (5, 7, 11), they are promising candidates for high resolution structure determination and structure-function analyses.

The physiological role of prokaryotic Na_Vs may be related to pH homeostasis, motility, and chemotaxis (6, 12). Searching bacterial genomic data bases, we found 26 sequences of putative NaChBac homologues from bacteria living in various environments. We were able to clone the putative Na_V genes from three of these bacteria, *Bacillus licheniformis*, *Shewanella putrefaciens*, and *Roseobacter denitrificans*, and named them Na_VBacL, Na_VSheP, and Na_VRosD, respectively. These homologues showed unique channel properties optimized for the specific environments in which the bacteria live.

We found an unexpected feature in the primary structure of Na_VSheP, namely a lack of glycine residues in helix S6. Crystal structures of potassium channels revealed that glycine and proline residues in helix S6 that are part of the "glycine hinge" and "PXP motif," respectively, create kinks in the open state (13–15). It has therefore been thought that these residues are critical for activation gating in tetrameric cation channels (15–19). Although Na_VSheP contains no glycine residues in helix S6, it still shows typical inward currents. To better understand their role, we mutated the glycine residues in helix S6 of Na_VBacL, Na_VRosD, and NaChBac to alanine. All mutants retained inward sodium currents. These results suggest that the previously proposed gating motifs are not obligatory for activation of prokaryotic Na_Vs.

The glycine mutations had no effect on activation but affected inactivation of the channels. Generally, voltage-gated cation channels are immediately inactivated after activation. Tetrameric cation channels have mainly two inactivation mechanisms, N-type and C-type inactivation (20–25). N-type

* This work was supported in part by Grants-in-Aid for Specially Promoted Research and the Japan New Energy and Industrial Technology Development Organization.

The nucleotide sequence(s) reported in this paper has been submitted to the DDBJ/GenBank™/EBI Data Bank with accession number(s) AB517991, AB517992, and AB517993.

[1] Supported by a fellowship from the Japan Society for the Promotion of Science.

[2] To whom correspondence should be addressed: Dept. of Biophysics, Graduate School of Science, Kyoto University, Oiwake, Kitashirakawa, Sakyo-ku, Kyoto 606-8502, Japan. Tel.: 81-75-753-4216; Fax: 81-75-753-4218; E-mail: yoshi@em.biophys.kyoto-u.ac.jp.

[3] The abbreviations used are: Na_V, voltage-gated sodium channel; K_V, voltage-gated potassium channel; MALDI, matrix-assisted laser desorption ionization; TOF, time-of-flight; CHO, Chinese hamster ovary; HEK, human embryonic kidney.

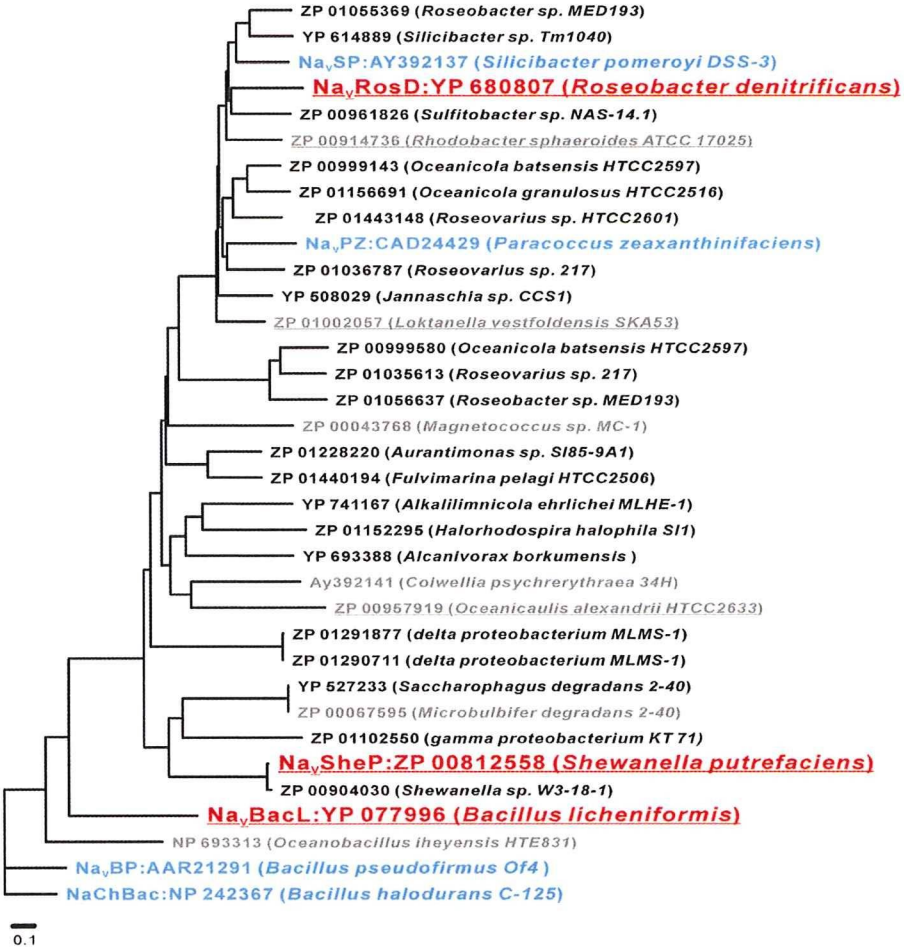

FIGURE 1. **Phylogenetic tree of bacterial NaChBac homologues.** A phylogenetic tree shows the bacterial species that express NaChBac homologues and their GenBank™ accession numbers. The program ClustalW was used to calculate a multiple sequence alignment based on conserved sequences of the NaChBac homologues. The phylogenetic tree was generated using the program PROTDIST, part of the PHYLIP package (Phylogeny Inference Package; available on the World Wide Web). The branch lengths are proportional to the sequence divergence, with the *scale bar* corresponding to 0.1 substitution per amino acid site. *Red underlined*, homologues that were newly cloned and functionally characterized in this study; *gray underlined*, homologues that could not be cloned in this study; *blue*, homologues that were functionally characterized previously; *gray*, homologues that were previously cloned but did not show detectable channel activity.

or fast inactivation is thought to be mediated by the interdomain linkers of Na_Vs or the N termini of voltage-gated potassium channels, a mechanism described by the "ball and chain" model (20–22). Although C-type inactivation is common in tetrameric cation channels, its molecular mechanism remains unclear. It has been proposed that C-type inactivation may be related to a collapse of the selectivity filter (23–25). Prokaryotic Na_Vs lack an obvious cytoplasmic N-type inactivation peptide, and inactivation may thus only occur through the C-type inactivation mechanism (25, 26). Furthermore, comparative studies and mutational analysis of these new Na_V homologues provide evidence that the rate of C-type inactivation is affected by the residues of helix S6.

EXPERIMENTAL PROCEDURES

Cloning of NaChBacs Homologues and Site-directed Mutagenesis—The NaChBac amino acid sequence (NP_242367) was used as a query for a BLASTP search against the Microbial Genomic data base at NCBI. The identified primary sequence data were obtained from Entrez at NCBI (*B. licheniformis* ATCC 14580 DSM 13 as NC_006270, *Loktanella vestfoldensis* SKA53 as NZ_AAMS01000001, *Rhodobacter sphaeroides* ATCC 17025 as NZ_AAME01000021, *S. putrefaciens* CN-32 as NZ_AALB00000000, *R. denitrificans* OCh 114 as NC_008209, and *Oceanicaulis alexandrii* HTCC2633 as NZ_AAMQ01000008). Samples of *B. licheniformis* (Japan Collection of Microorganisms number 2505), *L. vestfoldensis* (Japan Collection of Microorganisms number 21637) and *R. sphaeroides* (Japan Collection of Microorganisms number 6121) were obtained from the RIKEN BioResource Center. Samples of *S. putrefaciens* (National Institute of Technology and Evaluation Biological Resource Center number 3908), *R. denitrificans* (National Institute of Technology and Evaluation Biological Resource Center number 15277), and *Oceanicaulis* sp. (National Institute of Technology and Evaluation Biological Resource Center number 101722), closely related to *O. alexandrii* by 16 S rRNA sequence analysis, were obtained from the National Institute of Technology and Evaluation. DNAs of NaChBac homologues were directly cloned by PCR from colonies of bacteria using PrimeSTAR® GXL DNA Polymerase (Takara Bio.).

The following primers were used for cloning: 5′-CGCGGATCCATGAACACTCATCAAAATCGA-3′ and 5′-CGCGGATCCATCTTTCTTTTCATTTTGGGT-3′ for *B. licheniformis*; 5′-CGCGGATCCATGAGTACATCTTTACTT-3′ and 5′-CGCGGATCCGTCAGAACCAATGTTTCC-3′ for *S. putrefaciens*; 5′-CGCGGATCCATGGGTGTAAGAGAGCAA-3′ and 5′-CGCGGATCCGGACCGGGGCCTGTCTTT-3′ for *R. denitrificans*; 5′-CGCGGATCCATGAATTTGCGCGCCAGAACA-3′ and 5′-CGCGGATCCCTTGCCCGCCTGATCCAGTCG-3′ for *L. vestfoldensis*; 5′-CGCGGATCCATGACAGTGCGGGAAATGGTA-3′ and 5′-CGCGGATCCGCCGCGCGTCTCGTCGCCCGC-3′ for *R. sphaeroides*; and 5′-CGCGGATCCATGAGCGACGCGTCGGCC-3′ and 5′-CGCGGATCCCTCGGAATTGTCCGCCCG-3′ for *O. alexandrii*.

PCR products were cloned into a modified pET21b plasmid (Novagen) using BamHI restriction sites. These cloned DNAs contained additional methionine, glycine, and serine codons

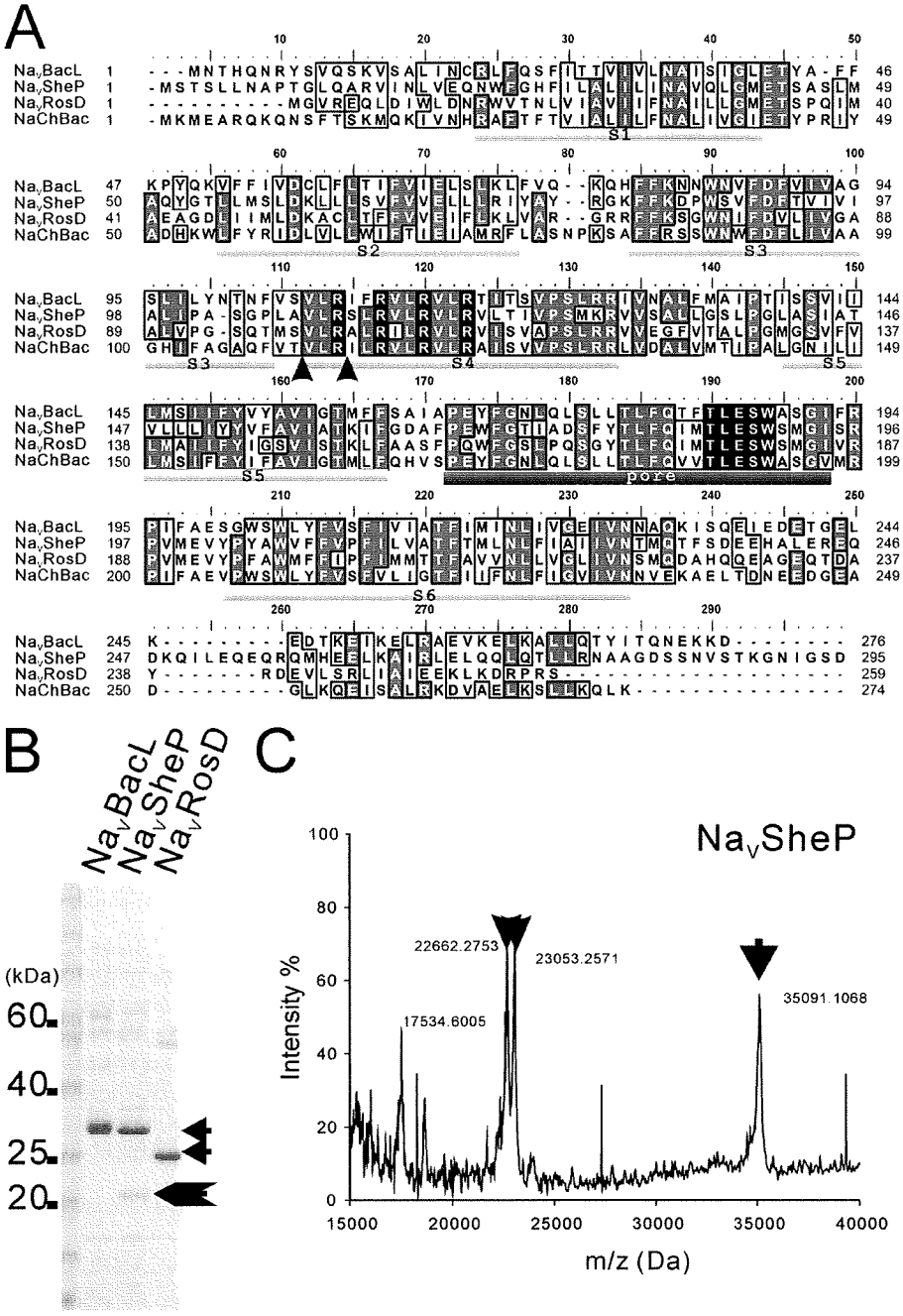

FIGURE 2. **Primary structures and expression of NaChBac homologues.** *A*, alignment of the deduced amino acid sequences of Na_VBacL, Na_VSheP, Na_VRosD, and NaChBac. The six putative transmembrane domains (S1–S6) are *underlined* in *light gray*, and the putative pore region is *underlined* in *dark gray*. Conserved arginines in helix S4 implicated in voltage sensing and residues constituting the putative sodium selectivity filter are shown as *white letters* in *black boxes*. The *arrowheads* indicate cleavage sites in Na_VSheP identified by MALDI mass spectrometry. *B*, Coomassie-stained SDS-PAGE of Na_VBacL, Na_VSheP, and Na_VRosD purified by Co^{2+} affinity chromatography. *C*, MALDI-TOF peptide mass spectrum of purified Na_VSheP. The *x* axis represents the mass-to-charge ratio (*m/z*), and the *y* axis represents relative abundance. The *arrow* indicates the full-length NaChBac homologues, and the *arrowheads* indicate fragments of Na_VSheP.

before the first methionine and a thrombin cleavage site before the C-terminal His tag. For expression in mammalian cells, three NaChBac homologues (Na_VBacL from *B. licheniformis*, Na_VSheP from *S. putrefaciens*, and Na_VRosD from *R. denitrificans*) were subcloned into the pCI vector (Promega) using the NheI and KpnI sites. Site-directed mutagenesis was accomplished by PCR of the full-length pCI plasmid containing the Na_V gene using high fidelity *Pfu* DNA polymerase (method by Stratagene). All clones were confirmed by DNA sequencing.

Expression and Purification of Recombinant Prokaryotic Na_Vs—Proteins were expressed in *E. coli* BL21 Δstar™ (DE3) (Invitrogen). 100 ml of LB medium (Invitrogen) containing 100 μg/ml ampicillin (Wako) was inoculated with 10 μl of glycerol stock and incubated overnight at 37 °C. 12.5 ml of the saturated culture medium was then used to inoculate 1.25 liters of LB medium containing 40 μg/ml ampicillin, and cells were grown at 37 °C to an A_{600} of 0.8. Cells were induced with 0.5 mM isopropyl 1-thio-β-D-galactopyranoside (Wako) and grown for 16 h at 18 °C. Cells were suspended in TBS buffer (20 mM Tris-HCl, pH 7.4, 300 mM NaCl) and lysed using a French press (SLM AMINCO) at 12,000 p.s.i. Membranes were collected by centrifugation (100,000 × *g*, 1 h, 4 °C) and solubilized by homogenization in TBS buffer containing 40 mM CYMAL-5 (Anatrace). After centrifugation (40,000 × *g*, 30 min, 4 °C), the supernatant was loaded onto a HIS-Select® cobalt affinity gel column (Sigma). The column was washed with 10 mM imidazole in TBS buffer containing 8 mM CYMAL-5, and the protein was eluted with 300 mM imidazole. Purified proteins were resolved on 10–20% SDS-PAGE gradient gels (Wako) and stained with Coomassie Blue. The BenchMark™ prestained protein ladder (Invitrogen) was used as molecular weight markers.

Mass Spectrometry—Mass spectrometry was carried out with a MALDI-TOF instrument (Voyager-DE, Applied Biosystems), using α-cyanohydroxycinnamic acid (Sigma) as matrix. Protein samples were mixed with the same volume of 90% acetonitrile (Wako) and 0.2% trifluoroacetic acid (Sigma), loaded onto a sample plate, dried, and washed with deionized water. Finally, 1% α-cyanohydroxycinnamic acid dissolved in 50% acetonitrile and 0.1% trifluoroacetic acid was

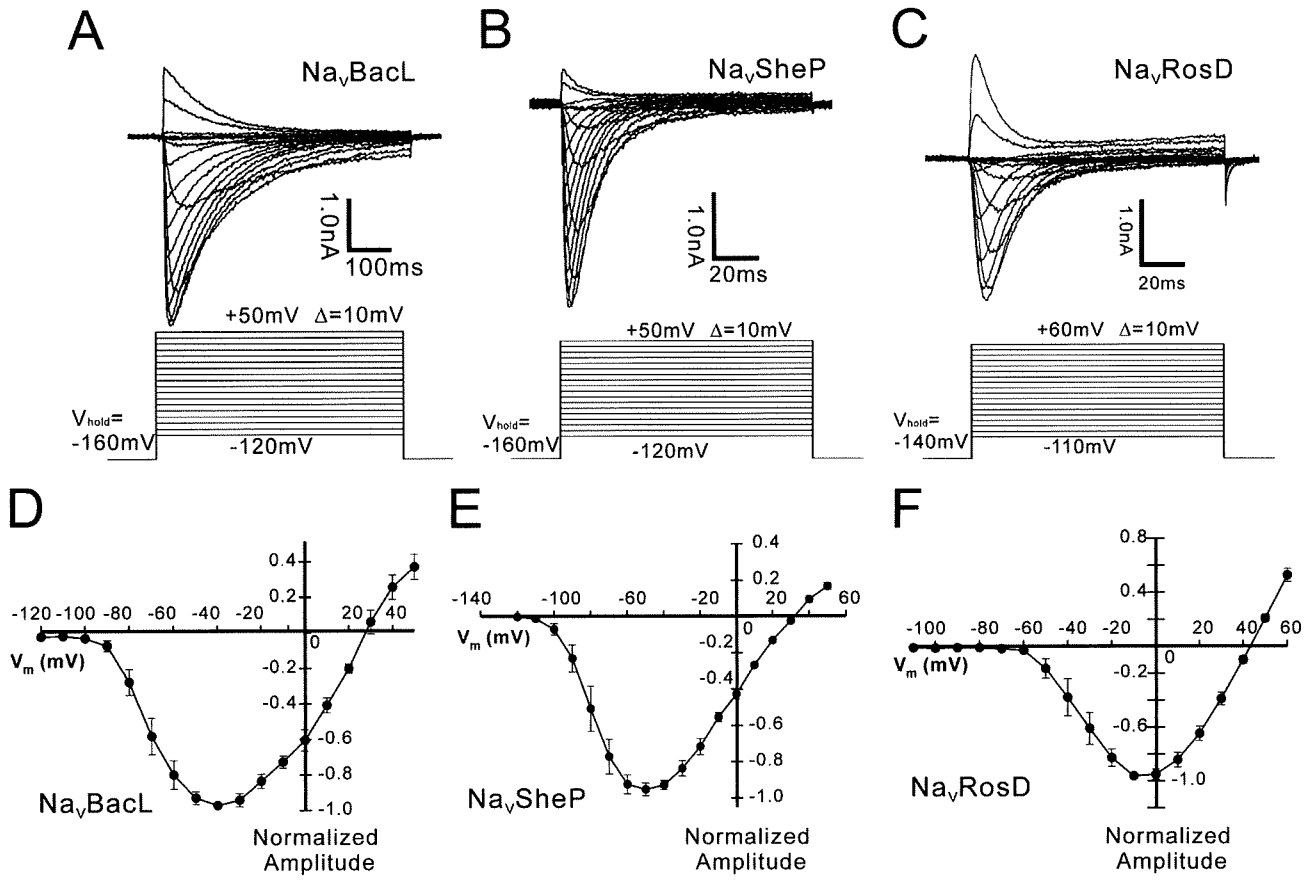

FIGURE 3. **Functional expression of Na_VBacL, Na_VSheP, and Na_VRosD in HEK 293 cells.** *A–C*, representative traces of $I_{NaVBacL}$, $I_{NaVSheP}$, and $I_{NaVRosD}$ resulting from the voltage protocol shown *below* (*D–F*). Averaged ($n = 7$; ±S.E.) peak current-voltage (*I/V*) relation of Na_VBacL, Na_VSheP, and Na_VRosD normalized by the peak current. V_{Hold} indicates the holding potential. The intersweep interval was 15 s.

loaded onto the dried samples. Mass spectra were collected using the delayed extraction mode.

Mammalian Electrophysiology—Chinese hamster ovary (CHO)-K1 or human embryonic kidney (HEK) 293 cells were grown in Dulbecco's modified Eagle's medium (Sigma) complemented with 10% fetal bovine serum (BioWhittaker), 100 units/ml penicillin (Invitrogen), and 100 μg/ml streptomycin (Invitrogen) at 37 °C under 5% CO_2. Cells were transfected with Na_V and pEGFP DNA using the calcium phosphate transfection kit (Invitrogen) and plated onto coverslips. Currents were recorded 12 h (Na_VBacL and Na_VSheP) or 36 h (Na_VRosD and NaChBac) after transfection. The pipette solution contained 105 mM CsF, 35 mM NaCl, 10 mM EGTA, and 10 mM HEPES (pH 7.4). The bath solution contained 150 mM NaCl, 1.5 mM $CaCl_2$, 1 mM $MgCl_2$, 2 mM KCl, 10 mM HEPES (pH 7.4), and 10 mM glucose. For measurements of the voltage dependence of Na_VBacL and Na_VSheP, 150 mM NaCl in the bath solution was replaced by 75 mM NaCl and 75 mM *N*-methyl-D-glucamine. All experiments were conducted at 25 ± 2 °C. Nifedipine (Sigma) was dissolved in DMSO (Wako). The final concentration of the solvent was less than 1%. Whole-cell patch clamp recordings of wild-type NaChBac confirmed that 1% DMSO did not affect the channel activity. All chemicals were dissolved in water. All other compounds were applied to the cultured cells using a perfusion system. For pharmacological measurements, cells were perfused with bath solution containing the inhibitors for 5 min prior to recording currents. All results are presented as mean ± S.E. A simple comparison between Na_VBacL wild type and G201A was made by Student's *t* test. To assess statistical differences in time constants between wild type and mutant proteins, multiple comparisons were made by one-way analysis of variance followed by the Tukey-Kramer multiple comparisons test.

RESULTS

We used the full NaChBac sequence for a standard BLASTP search against the GenBank™ data base of prokaryotic genomic sequences. The BLASTP search yielded 34 sequences that contained both a "TLESW" sequence, the putative selectivity filter of prokaryotic sodium channels (5–7), and positively charged amino acids at every third position in helix S4, the hallmark of voltage sensors (3, 5) (Fig. 1). The channel activity of four of the identified homologues (NaChBac as NP242367, Na_VBP as AAR21291, Na_VPZ as CAD24429, and Na_VSP as AY392137) had already been established (5–7), whereas four other homologues (NP 693313 of *Oceanobacillus iheyensis* HTE831, ZP 00067595 of *Microbulbifer degradans* 2-40, Ay392141 of *Colwellia psychrerythraea* 34H, and ZP 00043768 of *Magnetococcus* sp. *MC-1*) showed no channel activity in previous studies (7). Of the bacteria containing the remaining 26